

# **Microfluidic sensing and power generation with coplanar interdigital capacitors**

by  
Zhaochu Yang



Thesis submitted for the degree  
of Philosophiae Doctor

Faculty of Mathematics and Natural Sciences  
University of Oslo

Spring 2015

© **Zhaochu Yang, 2015**

*Series of dissertations submitted to the  
Faculty of Mathematics and Natural Sciences, University of Oslo  
No. 1666*

ISSN 1501-7710

All rights reserved. No part of this publication may be  
reproduced or transmitted, in any form or by any means, without permission.

Cover: Hanne Baadsgaard Utigard.  
Print production: John Grieg AS, Bergen.

Produced in co-operation with Akademika Publishing.  
The thesis is produced by Akademika Publishing merely in connection with the  
thesis defence. Kindly direct all inquiries regarding the thesis to the copyright  
holder or the unit which grants the doctorate.

# Abstract

Microfluidics is considered as both science and technology that deal with fluids in microchannels or in micro scale space. During the past two decades, microfluidic has been the hot spot in various research areas, e.g., biomedical assay, microchemical system, thermal management of electronic device, micro-electro-mechanical systems, etc., due to the emergences of various microfluidic devices. Transduction and sensing for microfluids therefore attract numerous interests from the diverse fields. Interdigital capacitance comprising of interdigital electrodes (IDEs) and thin insulation film provides a feasible solution for microfluidic transduction. Particularly, it has coplanar configuration and can be easily realized by use of microfabrication processes. Hence, it is of great interest to integrate the interdigital capacitance into a microsystem device for microfluidic transduction. This thesis explores the promising applications of interdigital capacitance for microfluidic generation and sensing.

Due to its inherent flexibility, fluidic energy harvester has obtain many attentions. The conventional electrostatic energy harvesters have been proposed to convert the ambient vibration to electric energy, often seen with solid spring-mass configurations. The spring-mass structure takes full advantages of resonant vibration to give maximum output power at a narrow frequency band; however, it in the meantime brings challenges to be adapted for wideband and low frequency applications. To overcome these challenges, a fluidic electrostatic energy harvester is proposed with employment of interdigital capacitance with a thin PTFE film deposited by sputtering process. Owing to charges embedded inside the dielectric film, no extra charging process is required. When a conductive droplet or ionic liquid marble rolls across the interdigital capacitance, this fluidic energy harvester can output an electric power.

Capacitance variation and open circuit voltage of the fluidic energy harvester was determined by finite element method (FEM) simulation when the droplet was at different position with respect to the IDEs. The charges on the IDEs were also checked. It is found that when the IDEs with given dimensions of finger/gap width, the total capacitance variation increases rapidly with the increase of droplet size to a peak value, and then drops as the

droplet size keeps increasing, even turning to be negative when the droplet size is big enough to cover more than one pair of fingers.

Microfabrication processes have been used to fabricate a prototype of this fluidic energy harvester. Experimental investigations of the fluidic energy harvester were conducted with both mercury droplet and ionic liquid marble. With a 1.2-mm mercury droplet rolling across the electret film of the prototype, a maximum output power was obtained at 0.18  $\mu\text{W}$  and the peak value of the output voltage was 1.5 V. A semi-empirical model was developed to understand the output waveforms. Several factors influencing the output performance are discussed. This fluidic electrostatic energy harvester is especially suitable for very low frequency vibration up to a few Hz.

To explore the sensing capability of interdigital capacitance for microfluids, a microfluidic flow pattern sensor was also proposed and demonstrated, in which the insulation film was made of SU-8 rather than PTFE film. This microfluidic flow pattern sensor operates on capacitance variation corresponding to different flow regime passing across the sensing area. The prototype of the flow pattern sensor composed of the glass substrate, IDEs covered by the thin insulation film, and the PDMS cover, therefore to form a microchannel.

Experimental investigation on the microfluidic flow pattern sensor was performed by use of deionized water and olive oil. The capacitance variation was characterized corresponding to 3 typical flow patterns, namely, droplet flow, short slug flow, and long slug flow. According to the data of time-dependent capacitance variation, both velocity and size of the flow regime can be determined due to that the sensing length of the sensor is known. The constants specific to each flow pattern are calculated so that the microfluidic flow pattern can be easily identified. This microfluidic flow pattern sensor can be easily integrated into complicated microsystems as all the fabrication processes are compatible.

With the demonstrations of fluidic electrostatic energy harvester and microfluidic flow pattern sensor, we may conclude that interdigital capacitance is very promising for microfluidic generation and sensing, due to the coplanar configuration and the capability of non-invasive operation.



# Preface

This thesis is submitted in partial fulfilment of requirements for the degree of Philosophiae Doctor from the Department of Mathematics, Faculty of Mathematics and Natural Sciences at University of Oslo (UiO), Norway.

The work has been conducted from November 2009 to December 2014 in the Institute of Micro and Nano Systems Technology at Buskerud and Vestfold University College (HBV), Horten, with Professor Einar Halvorsen, Ph.D., as the primary supervisor from HBV and with co-supervisors Associate Professor Tao Dong, Ph.D., from HBV and Professor Atle Jensen, Ph.D., from UiO.

This work was funded by the Research Council of Norway under grant number 191282.



# Acknowledgement

I would like to express my sincere gratitude and appreciation to all those who supported me toward completing this thesis.

Most of all, my sincere gratitude goes to my primary supervisor Professor, Einar Halvorsen, Ph.D., for his valuable guidance and advice during my Ph.D. project. I am especially grateful for his tireless encouragement, motivation and priceless advice on my scientific work. I would also like to express my sincere gratitude to my co-supervisors, Associate Professor Tao Dong, Ph.D. and Professor Atle Jensen, Ph.D., who have provided great advice, input, motivation and feedback during my project work. They have also supported and inspired me throughout my thesis work with their patience and expertise.

I am grateful to the Department of Micro and Nano Systems Technology (IMST), Faculty of Technology and Marine Studies (TekMar) at Buskerud and Vestfold University College (HBV), for the useful facilities. Especially, I would like to thank Mr. Dahl Johansen and Ms. Zekija Ramic for their supports in my experimental work.

My appreciation should not be forgotten for my colleagues in energy harvesting group, especially, Lars-cyril Blystad, Ph.D., Duy Son Nguyen, Ph.D., Cuong Phu Le, Ph.D., and Sukhdeep Kaur., Ph.D. candidate. Their helps and the experiences with them have impressed me on my memory. My appreciation also goes for my friends and colleagues in IMST, including Nuno Pires, Ph.D., Xinyan Zhao, Ph.D. candidate, Haakon Karlsen, Ph.D. candidate, Zhongqiang Li, Ph.D. candidate, and some master students, for their encouragement during my doctoral work.

Finally, but by no means least, my deepest thanks are extended to my family in China. Their continuous supports from all aspects have been always encouraging me to go that far for my academic career.



# Contents

<b>Abstract</b> .....	<b>I</b>
<b>Preface</b> .....	<b>III</b>
<b>Acknowledgement</b> .....	<b>V</b>
<b>Contents</b> .....	<b>VII</b>
<b>List of Figures</b> .....	<b>IX</b>
<b>List of Tables</b> .....	<b>XI</b>
<b>Chapter 1 Introduction</b> .....	<b>1</b>
1.1 Background: Microfluidics .....	1
1.1.1 Continuous-flow microfluidics .....	2
1.1.2 Droplet-based microfluidics .....	2
1.1.3 Digital microfluidics .....	3
1.1.4 Microfluidic cooling for electronic devices .....	3
1.1.5 Microfluidics coupled with other physical fields .....	4
1.2 Interdigital capacitance (IDC).....	4
1.2.1 Interdigital electrodes .....	4
1.2.2 Insulation layer (Passivation layer).....	5
1.2.3 Analytical model of interdigital capacitance.....	6
1.3 Energy harvesting.....	7
1.3.1 Fundamentals of energy harvesting.....	7
1.3.2 Electrostatic energy harvester .....	9
1.4 Microfluidic two-phase flow .....	12
1.4.1 Microfluidic gas-liquid flow .....	12
1.4.2 Microfluidic liquid-liquid flow .....	13
1.5 Main work of the thesis .....	15
<b>Chapter 2 Fluidic electrostatic energy harvester</b> .....	<b>17</b>
2.1 Overview of fluidic electrostatic energy harvester .....	17
2.2 Working principle and modeling.....	19
2.2.1 Working principle .....	19
2.2.2 Modeling .....	20
2.3 Simulation .....	21

2.3.1 Physical model .....	21
2.3.2 Simplifying assumptions .....	22
2.3.3 Simulation domain and procedure .....	23
2.4 Prototype fabrication and test .....	24
2.4.1 Microfabrication of the prototype .....	24
2.4.2 Test setup .....	25
2.5 Results .....	27
2.5.1 Simulation results .....	27
2.5.2 Test results .....	28
<b>Chapter 3 Microfluidic two-phase flow pattern sensor .....</b>	<b>37</b>
3.1 Overview of microfluidic two-phase flow sensing .....	37
3.2 Working principle .....	39
3.3 Simulation of capacitance sensor for air-water two-phase flow .....	42
3.3.1 Simulation model and settings .....	42
3.3.2 Simulation results .....	43
3.4 Prototype of two-phase flow pattern sensor design and fabrication .....	45
3.4.1 Design considerations .....	45
3.4.2 Design and microfabrication .....	46
3.5 Experiment of oil-liquid two-phase flow .....	47
3.5.1 Experimental setup and test procedure .....	47
3.5.2 Capacitance-to-Digital Converter .....	48
3.5.3 Data acquisition .....	48
3.6 Experimental results of oil-water two-phase flow pattern sensing .....	49
3.6.1 Typical oil-water two-phase flow patterns .....	49
3.6.2 Typical capacitance variation with respect to typical flow patterns .....	50
3.6.3 A characteristic number distinguishing flow patterns .....	54
<b>Chapter 4 Conclusions and prospects .....</b>	<b>57</b>
4.1 Conclusions .....	57
4.2 Prospects .....	58
<b>Chapter 5 List of publications .....</b>	<b>61</b>
<b>References .....</b>	<b>113</b>

# List of Figures

Figure 1.1 Similarity between the interdigital capacitance and the parallel-plate capacitance: (a) a parallel-plate capacitor; (b) one pair of coplanar electrodes; (c) interdigital capacitance comprising of more electrode pairs. ....	4
Figure 1.2 The dielectric layer coating the electrodes: the thickness can be changed while the polymer undergoes adsorption/absorption processes for chemical sensor. Reprinted from Ref. [58], Copyright (2006), with permission from Elsevier. ....	5
Figure 1.3 Comparison of energy sources and output performance. ....	8
Figure 1.4 Comparison of typical energy harvesting systems by Yildiz (2009).....	8
Figure 1.5 Basic configurations of electrostatic energy harvester (Reprinted from Ref. [82], Copyright (2002), with permission from ASME): (a) In-plane overlap varying; (b) In-plane gap closing; (c) Out-of-plane gap closing. ....	10
Figure 1.6 Another basic configuration of electrostatic energy harvester, in-plane variable surface by Boisseau et al. (2012): (a) full plate variable; (b) patterned surface variable.....	10
Figure 1.7 Typical electrostatic energy harvesters: (a) an electrostatic constant charge harvester for wideband operation from Imperial College, UK, Reprinted from Ref. [91], Copyright (2006), with kind permission from Springer Science and Business Media; (b) an electret-based converter for 3D energy harvesting from Furtwangen University, Germany, Reprinted from Ref. [84], Copyright (2011), with permission from SPIE. ....	11
Figure 1.8 Flow focusing to generate monosized microbubbles [102], Copyright (2001) by The American Physical Society. ....	12
Figure 1.9 Geometric structures of microfluidic devices for droplet formation: (A) T-junction; (B) Flow-focusing; (C) Co-flowing. Reprinted from Ref. [105], Copyright (2013), with permission from Elsevier. ....	14
Figure 1.10 Oil-water two-phase flow pattern in microchannels: (a) typical flow patterns (from top to bottom), slug flow, monodispersed droplets flow, droplets populations flow, parallel flow; (b) flow pattern map. Reprinted from Ref. [112], Copyright (2006), with permission from John Wiley and Sons.....	14
Figure 1.11 Different structures of the G/O/W double emulsions generated by adjusting the three phase flow rates. Reprinted from Ref. [113], Copyright (2012), with permission from Royal Society of Chemistry. ....	15
Figure 2.1 Status of fluidic electrostatic energy harvester research.....	19
Figure 2.2 Schematics of the working principle: (a) droplet covers one electrode; (b) droplet covers two electrodes; (c) equivalent capacitor network; (Reprinted with permission from [129]. Copyright 2012, American Institute of Physics.) (d) configuration of interdigital electrodes with contact pads A and B for external connection. ....	20
Figure 2.3 Electric circuit representation of the harvester and external components. ....	21
Figure 2.4 Droplet-based electrostatic energy harvester. (a) Optical photo of prototype; (b) Equivalent circuit characterizing the energy harvester. ....	22
Figure 2.5 Schematic drawing of simulation domain. ....	23

Figure 2.6 Meshing of the IDE fingers and thin insulation film (top view). .....	24
Figure 2.7 Schematic drawing of microfabrication process, not to scale: (a) Gold deposition; (b) Patterning IDEs; (c) Wet etching; (d) Magnetron RF sputtering; (e) PDMS baffle wall adhesion.....	24
Figure 2.8 Device under test: (a) Photo of prototype device mounted on a PCB; (b) Test condition.....	25
Figure 2.9 Liquid proof mass on interdigital electrode pattern: (a) photo of IL marble with a diameter of 1.2 mm on 500 $\mu\text{m}$ -wide electrode; (b) IL marble with a diameter of 1.2 mm on 400 $\mu\text{m}$ -wide electrode; (c) mercury droplet with a diameter of 1.2mm on 400 $\mu\text{m}$ -wide electrode under an optic microscope.....	26
Figure 2.10 Capacitance variation with droplet position. ....	27
Figure 2.11 Open-circuit potential variation with droplet position.....	27
Figure 2.12 Charges on the grounded electrodes. ....	28
Figure 2.13 Influence of droplet size on the capacitance variation.....	28
Figure 2.14 Output voltage with various external bias voltages utilizing metal ball: (a) Transient output voltage; (b) RMS output voltage.....	29
Figure 2.15 Accumulated output energy vs. time; Insets show corresponding instantaneous voltage: (a) mercury droplet, $D=1.2\text{mm}$ , inclination angle $\theta=20^\circ$ ; (b) IL marble, $D=1.2\text{mm}$ , inclination angle $\theta=15^\circ$ .....	30
Figure 2.16 Dynamic behavior of the mercury droplet rolling ( $D=1.2\text{mm}$ , inclination angle $\theta=15^\circ$ ).....	32
Figure 2.17 Dynamic behavior of the IL marble rolling ( $D=1.2\text{mm}$ , inclination angle $\theta=15^\circ$ ). .....	32
Figure 2.18 Spectrum of the output voltage with a mercury droplet ( $D=1.2\text{mm}$ , inclination angle $\theta=15^\circ$ ).....	33
Figure 2.19 Comparison of the modeling plots with the test data (Mercury droplet, $D=1.0\text{mm}$ , inclination angle $\theta=15^\circ$ ).....	33
Figure 2.20 The charge variation rate with respect to displacement, based on the test data with mercury droplet, $D=1.0\text{mm}$ , inclination angle $\theta=15^\circ$ .....	34
Figure 2.21 Accumulated output energy versus time for different dimensions of mercury droplet with inclination angle $\theta=15^\circ$ .....	35
Figure 2.22 Accumulated output energy versus time for different inclination angles ( $D=1.0\text{mm}$ ).....	36
Figure 3.1 Schematic of the two-phase flow patterns sensor.....	39
Figure 3.2 Typical oil-in-water two-phase flow patterns and the corresponding capacitance variation at different time points (flow direction: from left to right): (a) droplet flow; (b) short slug flow; (c) long slug flow. ....	40
Figure 3.3 Reduced length versus time ratio.....	42
Figure 3.4 Schematic drawing of the simulation model: (a) simulation domain; (b) dimensions of the IDE.....	43
Figure 3.5 Initial capacitance varies with the thickness of the insulation layer.....	44
Figure 3.6 Capacitance responses with respect to various liquid slug length.....	45



Figure 3.7 Relationship between the penetration length and the thickness of the liquid phase: (a) $T < hc$ ; (b) $hc < T$ .....	45
Figure 3.8 Prototype of flow pattern sensors: (a) Optic photo; (b) Prototype fixed on the PCB board with the electric connections via wire bonding.....	46
Figure 3.9 Experimental system setup: (a) Schematic arrangement; (b) Photo during the test. ....	47
Figure 3.10 Simplified functional diagram of the AD7746 Capacitance-to-Digital Converter, Analogy Digital [149].....	48
Figure 3.11 Typical flow patterns in the microchannel. (a) Droplet flow, $Q_o=0.001\text{mL/min}$ , $Q_w=0.005\text{mL/min}$ ; (b) Short slug flow pattern, $Q_o=0.003\text{mL/min}$ , $Q_w=0.03\text{ mL/min}$ . (c) Long slug flow pattern, $Q_o=0.004\text{ mL/min}$ , $Q_w=0.06\text{ mL/min}$ ; (d) Annular flow, $Q_o=0.005\text{ mL/min}$ , $Q_w=0.1\text{ mL/min}$ .....	49
Figure 3.12 Flow pattern map, with y- oil flow-rate and x-water flow-rate.....	50
Figure 3.13 Capacitance of droplet flow with sensor A (Flow enters the sensing area from the right to the left): (a) one sensing unit; (b) two sensing units.....	51
Figure 3.14 Capacitance variation of short slug flow with sensor A (Flow enters the sensing area from the right to the left): (a) one sensing unit; (b) two sensing units.....	52
Figure 3.15 Capacitance of long slug flow with sensor A: (a) one sensing unit; (b) two sensing units. (Flow enters the sensing area from the right to the left).....	53
Figure 3.16 Values of the constant that is directly related to the flow patterns. The square markers represent the average value of $D_0$ and the error bars represent the minimum and maximum values.....	55

## List of Tables

Table 1.1 Descriptions on microfluidics.....	1
Table 1.2 Available energy sources from the environment.....	7
Table 1.3 Comparison of vibration energy-harvesting techniques (Marzencki 2005).....	9
Table 2.1 Parameters of the simulation domain.....	23
Table 2.2 Comparison of acceleration from LSF vs. ideal value (Unit: $\text{m/s}^2$ ).....	32
Table 3.1 Geometrical parameters of IDEs.....	43
Table 3.2 Initial capacitance with different geometrical parameters of IDEs.....	44
Table 3.3 Geometrical Parameters of Capacitive Sensors.....	46



# Chapter 1

## Introduction

### 1.1 Background: Microfluidics

The powerful trend of miniaturization, enabling to manufacture ever smaller mechanical, optical, electronic devices, have brought profound innovations in human being's daily lives [1, 2]. As the main driving force of miniaturization, the microfabrication technologies originated from semiconductor industry, have been providing boundless possibilities for micro systems and micro devices, e.g., microphones in smart phones and portable electronics, accelerometers in modern cars, injecting printers, silicon pressure sensors, etc. [3]. A sub-category of the micro systems and devices are involved with fluids, such as, lab-on-a-chip (LOC) [4], micro total analysis system ( $\mu$ TAS) [5], micromixer [6], microreactors [7], etc. Therefore, a new subject, microfluidics, was formed.

Then a question rises naturally: *what is the exact description of microfluidics?* Several answers with respect to this question have been proposed, as summarized in Table 1.1.

Table 1.1 Descriptions on microfluidics

Author (Year)	Description	Key words
Stone and Kim (2001) [8]	Microfluidics refers to devices or flow configurations that have the smallest design feature on the scale of a micron or larger	Technology
Stone et al. (2004) [9]	Microfluidics refers to devices and methods for controlling and manipulating fluids with length scales less than a millimeter.	Technology
Whitesides (2006) [10]	Microfluidics is the science and technology of systems that process or manipulate small ( $10^{-9}$ to $10^{-18}$ litres) amounts of fluids, using channels with dimensions of tens to hundreds of micrometres.	Science and technology
Casadevall i Solvas and deMello (2011) [11]	Technology that exploits the atypical properties of fluids on the microscale.	Technology
Yeo et al. (2011) [12]	Microfluidics is the science of manipulating and controlling fluids and particles at micron and submicron dimensions and the technology associated with the development of methods and devices to undertake such.	Science and technology
Sackmann et al. (2014) [13]	Conceptually, the ideal of microfluidics is that fluids can be precisely manipulated using microscale device built with technologies first developed by the semiconductor industry and later expanded by the micro-electromechanical systems (MEMS) field.	Technology

According to Table 1.1, the common ground of the forgoing descriptions is that microfluidics manipulates fluids with *very small volume*. Nevertheless, as for how small it deserves to be called “microfluidics”, there are some inconsistencies: Stone et al. [9] defined microfluidics with the length scale at a micron or less than a millimeter; Yeo et al. [12] argued the micro and submicron dimensions while Sackmann et al. proposed the volume scales between atto litres ( $10^{-18}$  L) and femto litres ( $10^{-15}$  L). Such inconsistent descriptions may due to that the researchers came from diverse fields of application, who have different focuses on their own research.

Even though there is not a well-established definition, microfluidics has been considered both as a science (study of the behavior of fluids in microchannel or in microscale space) and a technology (manufacturing of microfluidics devices for applications). It is also recognized as an interdisciplinary subject, which involves in physics, chemistry, electronics, biology, mechanics, etc.

Although most current efforts in microfluidics concern devices with applications in chemistry, biology, and medicine [14], there are also several applications in the physical sciences for control systems and heat management, energy generation, display technology, etc. [15]. For convenience of description, we roughly sub-divide microfluidics into continuous-flow microfluidics, droplet-based microfluidics, and digital microfluidics, in terms of the flow features. However, this categorization is too rough to cover the whole picture of microfluidics research. Therefore, we supplemented another two subcategories as “Microfluidics cooling for electronic devices” and “Microfluidics coupled with other physical fields”.

### 1.1.1 Continuous-flow microfluidics

With the feature of maintaining continuous fluids flow inside the microfabricated channels, the continuous-flow microfluidics has seen widely applications in microchemical reaction [16], microchemical synthesis [17], cell separation and DNA purification [18], polymerase chain reaction (PCR) [19, 20], drug delivery [21], especially for those LOC and  $\mu$ TAS applications. The continuous flow can be driven by either external pressure gradient, integrated micropumps, or capillary forces combined with electrokinetic mechanism.

Due to the merits of small volume, miniature size, compactness, and versatility, the requirements from various biomedical applications have paved the way for the developments of microfluidics technology.

### 1.1.2 Droplet-based microfluidics

Differing from the continuous fluid flow in chips, the droplet-based microfluidics address discrete volume of fluids in immiscible phases, e.g., liquid-liquid flow, gas-liquid flow, even gas-liquid-liquid flow. In a broad sense, here the nomenclature droplet can refer to droplets, slugs, elongated slugs and even bubble and droplet of double-emulsions. Droplet-based

microfluidics allows isolation of single cells and reagents in monodisperse picoliter liquid capsules and manipulations at a throughput of thousands of droplet per seconds [22], resulting considerable benefits in synthesis, high-throughput screening, cell biology and systems biology [11].

The applications of droplet-based microfluidics range from fast analytical systems [23] or the synthesis of advanced materials [24] to protein crystallization [25] and biological assays for living cells. [26] Precise control of droplet volumes and reliable manipulation of individual droplets such as coalescence, mixing of their contents, and sorting in combination with fast analysis tools allow us to perform chemical reactions inside the droplets under defined conditions [27, 28].

### **1.1.3 Digital microfluidics**

Digital microfluidics (DMF) is an emerging liquid-handling technology that manipulates liquids in discrete droplets on surfaces by an electric potential applied to an array of electrodes in integrated microfluidic devices [29]. Even though there are some disagreement to the definition, DMF was more preferred to refer to the integrated systems in which droplets are manipulated on an array of electrodes, rather than systems in which droplets are manipulated in closed microchannels [30].

DMF allows automation and control of droplets unparalleled by any other technique of fluid transport, which makes it particularly attractive for low-volume applications involving a variety of bioanalytes [31], including enzyme assays, protein analysis [32], cell-based assays. Besides, DMF was developed into microfluidic logic gates based on two-phase flows at low Reynold's number [33], and well suitable for microscale sample processing for mass spectrum [34].

### **1.1.4 Microfluidic cooling for electronic devices**

Aside from the forgoing biomedical and chemical applications, efficient microfluidic cooling for high power density electronics has attracted increasing attention during the past decades. Since Tuckmann and Pease [35] firstly proposed microchannel heat sink for VLSI, considerable large heat fluxes with magnitudes up to 10,000 W/cm<sup>2</sup> have been achieved with microfluidic flow boiling heat transfer [36]. Recently, microfluidic cooling techniques have been developed for cooling of detectors [37], cooling of heterogeneous 3D IC applications [38], embedded cooling for high-flux electronic components [39], two-phase cooling of LED [40], etc. More recent advances on microfluidic for electronics cooling can be found in the review paper by Kandlikar (2014) [41].

### 1.1.5 Microfluidics coupled with other physical fields

It can be noticed that both continuous microfluidics and droplet-based microfluidics address more hydrodynamics of continuous or discrete fluids flow in micro scale than the other physical fields, while DMF inherently addresses the coupling of microfluidics with electric field. When combined with other physical fields, e.g., optics, acoustics, and magnetics, microfluidics can have extra interesting applications.

Combining the advantages of microfluidics and optics, optofluidics aims at manipulating fluids and light at the microscale and exploiting their interaction to create highly versatile systems [42]. Even though the term ‘optofluidics’ appeared less than ten years ago, it has applications including displays, biosensors, lab-on-chip devices [43], lenses, molecular imaging tools [44] and energy [45], etc.

Acoustofluidics, i.e., ultrasound-based external forcing of microparticles in microfluidics, has attracted particular attention because it allows gentle, label free separation based on purely mechanical properties: size, shape, density, and compressibility [46, 47, 48]. It can be used to move manipulate microparticles in microchannels.

To sum up, dealing with tiny volume of fluids, microfluidics has actually become a fascinating theme, which involves with interdisciplinary knowledge.

## 1.2 Interdigital capacitance (IDC)

### 1.2.1 Interdigital electrodes

Interdigital electrodes (IDEs), as the name indicates, is referred to digitlike or fingerlike periodic pattern of in-plane electrodes, see Figure 1.1(c). Since 1970’s, IDEs has been among the most commonly used periodic electrode configurations. The similarity between the interdigital capacitance and the parallel-plate capacitance is that the former can be considered as the results from the electrodes of the parallel-plate capacitance opening up to a coplanar state, as illustrated in Figure 1.1(a), (b).

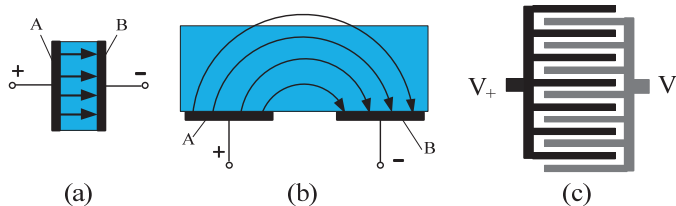


Figure 1.1 Similarity between the interdigital capacitance and the parallel-plate capacitance: (a) a parallel-plate capacitor; (b) one pair of coplanar electrodes; (c) interdigital capacitance comprising of more electrode pairs.

As the capacitance between one electrode pair is comparable to the stray capacitance of the leads, the coplanar electrode pairs have to repeat many periods to form a measurable structure. Therefore, the IDEs often comprise more finger pairs as shown in Figure 1.1(c). The number of the electrode pairs is one of the key parameter for interdigital capacitance.

Building up the capacitance associated with the electric fields that penetrate into material under test (MUT) or sensitive coating, IDEs have been involved in the fields such as, dielectrometry sensors [49], chemical sensors [50], humidity sensors [51, 52], surface acoustic wave transducers [53], and microelectromechanical systems (MEMS) [54], etc.

The benefits from the coplanar feature of IDEs can be summarized as below,

- (a) Easy to manufacture. The IDEs can be realized on printed circuit board (PCB) [55], or by electroplating to deposit a uniform layer of copper on the surface of Cu-Flon substrate [56]. Especially, electron beam thermal evaporation process followed by a conventional mask etching allows to control the deposition rate and thickness of electrodes, which is compatible with the follow-up microfabrication processes.
- (b) Not like the parallel-plate capacitor, the interdigital capacitance does not require two-sided access to the MUT. Such single-side access allows IDC to be integrated into a complicated system as a transducing or sensing component.

### 1.2.2 Insulation layer (Passivation layer)

Typically, a thin insulation layer (passivation layer) is often deposited to coat the electrodes for the sensors with IDEs, as shown in Figure 1.2. It helps to insulate the electrode fingers, or prevent cross contamination as the passivation layer [57]. Especially for chemical sensor with IDEs, the dielectric thin layer functions as the selective sensitive layer that responds to the changes in the concentration of certain specific type of molecules and ions present in the ambient fluid [56]. After undergoing the processes of analyte adsorption on the polymer surface, absorption into the polymer phase and swelling of the polymer layer, both permittivity and thickness of the dielectric layer will change, therefore changing the capacitance of sensor.

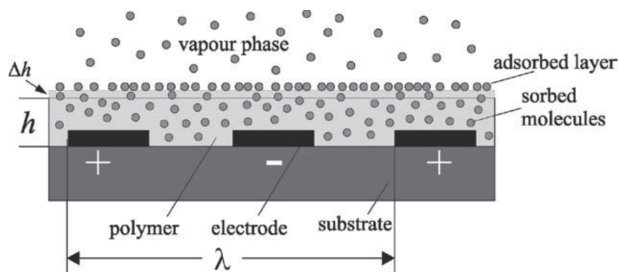


Figure 1.2 The dielectric layer coating the electrodes: the thickness can be changed while the polymer undergoes adsorption/absorption processes for chemical sensor. Reprinted from Ref. [58], Copyright (2006), with permission from Elsevier.

For chemical sensing, the reversibility of the dielectric thin layer is the main concern when the polymer layer was used for augmentation of signal strength. While for the sensing principle in which the polymer layer is only applied for insulation purpose, the stability of the dielectric thin layer is more concerned. In this case, the dielectric layer thickness, which can influence the sensor capacitance, is one of the key parameters.

It should be noted that even though polymers are widely used as the dielectric layer/passivation layer, some other dielectric materials can also be used, depending the specific purpose. For example, the metal-oxide nanoporous films (SnO<sub>2</sub>) was realized to detect the ethanol gas [59]; Zeolite-coated interdigital capacitors for humidity sensing [52].

### 1.2.3 Analytical model of interdigital capacitance

Estimation of the interdigital capacitance becomes important while designing a transducer/sensor with IDEs. 3D numerical simulation of interdigitated capacitors to optimize the sensor sensitivity was reported by Jungreuthmayer et al. [60]. Besides, several investigations on the analytical model of interdigital capacitance have been proposed.

Gevorgian et al. [61] used the conformal mapping technique to evaluate closed form expressions for computation of capacitances of IDC on two- and three- layered substrates. The derivation was based on the partial capacitance method, with consideration of the capacitance between the fingers and the fringing capacitance of the finger ends.

Memishev et al. [62] developed analytical expressions for the simple case of a Maxwell parallel-plate capacitor and contrasted with parametric numerical models of interdigital sensor probes. The visualization of those parametric spaces helps to develop intuition and understanding of dielectric measurement results in more complex cases.

Chen et al. [63] computed the capacitance corresponding to a pair of semi-infinite electrodes, which introduces two important design variables for sensor design, namely the field penetration depth and the effective electrode width. A reliable estimation of the capacitance for a coplanar electrode pair of finite width provided  $w/a \gg 1$  can be calculated by,

$$C = \frac{2\epsilon_r \epsilon_0 l}{\pi} \ln \left[ (1+w/a) + \sqrt{(1+w/a)^2 - 1} \right], \quad (1.1)$$

And the penetration depth is,

$$T = a \sinh \left[ \cosh^{-1} (1+w/a) \right] = a \sqrt{(1+w/a)^2 - 1} \quad (1.2)$$

In (1.1) and (1.2),  $w$  is the electrode width;  $a$  is half width of the electrode gap; and  $l$  is the overlap length. However, it was assumed that the non-conductive liquid directly contacted with the electrodes and no dielectric layer was considered in the model.

Based on conformal mapping techniques, Igreja and Dias [64] proposed new analytical expressions for the capacitance between the two comb electrodes of a periodic interdigital capacitive sensor. It was independent of the particular application and can be applied for any



space and finger width as well as for any number of layers with different thickness and permittivity. This analytical model gives excellent estimation when the permittivity of consecutive layers monotonically decreases from layer to layer (as moving away from the electrodes plane). Later, Igreja and Dias [65] further extended their model for the cases where there is a decrease in the permittivity from layer to layer, by splitting the concept of partial capacitance in parallel partial capacitance and serial partial capacitance. A more robust model was achieved giving accurate results for the most used structures with IDEs.

According to the available literatures, there is not a universal analytical model that can precisely estimate the interdigital capacitance for all the cases yet. As for a specific application, the forgoing analytical model may provide a rough estimation of capacitance; a precise determination of the interdigital capacitance can be achieved by FEM simulation or measurement technique.

## 1.3 Energy harvesting

### 1.3.1 Fundamentals of energy harvesting

Harvesting or scavenging energy from the environment and converting to electricity directly to power for small and mid-sized devices, such as autonomous wireless sensor nodes, consumer electronics, and portable electronics, have been attractive techniques since last decades [66-70]. With energy harvesting technology, such devices can be self-sufficient without external charging. Especially, rapid developments of intelligent wearable electronics [71], smart devices (e.g. smart watches [72]) and Internet-of-Things (IoT) [73] during the recent years, which involves in increasing utilization of low-power sensors and electronics, find more applications of energy harvesting in numerous critical areas from biomedical, agricultural, structural health monitoring to logistics, localization, and security. The available energy sources that are possible for harvesting from the environment are summarized in Table 1.2 [69, 74].

Table 1.2 Available energy sources from the environment

Energy source	Possible energy conversion principles
<b>Mechanical energy</b> (object motion and vibration, e.g., wind, water flow, ocean waves)	Electromagnetic, electrostatic or piezoelectric
<b>Solar and light energy</b> (outdoor sunlight and indoor room light)	Photovoltaic
<b>Thermal energy</b> (Waste heat energy variations from furnaces, heaters, and friction sources)	Thermoelectric, pyroelectric
<b>Electromagnetic radiation energy</b> (Base stations, wireless internet, radio, TV, etc.)	Electromagnetic
<b>Human body</b> (motion, temperature difference, etc.)	Electromagnetic, electrostatic, piezoelectric or thermoelectric

### 1.3 Energy harvesting

Figure 1.3 compared typical energy sources from the ambient and their performance [75]. Besides, the challenges for energy sources are described as well.


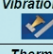

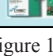
Energy Source	Challenge	Typical Electrical Impedance	Typical Voltage	Typical Power Output
 <b>Light</b>	Conform to small surface area; wide input voltage range	Varies with light input Low $k\Omega$ to 10s of $k\Omega$	DC: 0.5V to 5V [Depends on number of cells in array]	10 $\mu$ W-15mW (Outdoors: 0.15mW-15mW) (Indoors: <500 $\mu$ W)
 <b>Vibrational</b>	Variability of vibrational frequency	Constant impedance 10s of $k\Omega$ to 100k $\Omega$	AC: 10s of volts	1 $\mu$ W-20mW
 <b>Thermal</b>	Small thermal gradients; efficient heat sinking	Constant impedance 1 $\Omega$ to 100s of $\Omega$	DC: 10s of mV to 10V	0.5mW-10mW (20°C gradient)
 <b>RF &amp; Inductive</b>	Coupling & rectification	Constant impedance Low k $\Omega$ s	AC: Varies with distance and power 0.5V to 5V	Wide range

Figure 1.3 Comparison of energy sources and output performance.

Figure 1.4 compares the typical energy harvesting systems with different working principles, namely, electromagnetic, piezoelectric, electrostatic, thermoelectric and photovoltaic [74]. Additionally, some other principles, such as, pyroelectric energy harvesting for self-powered nuclear reactor wireless sensor networks have been reported [76].

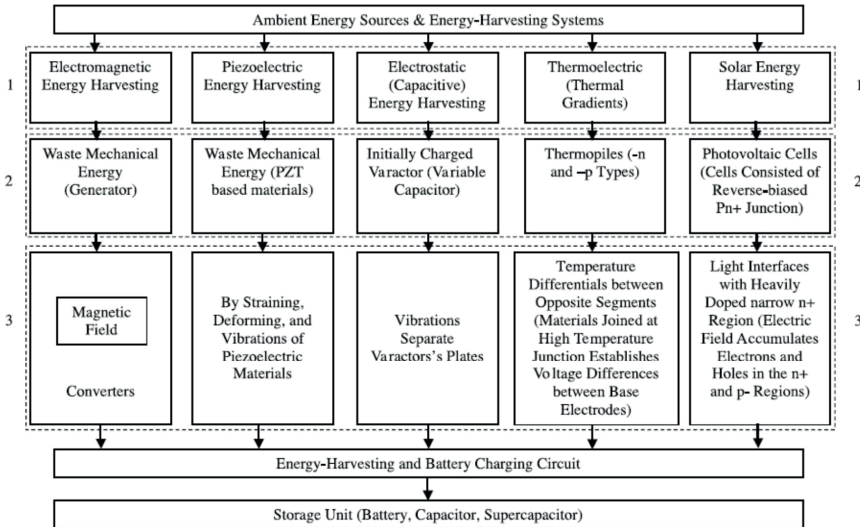


Figure 1.4 Comparison of typical energy harvesting systems by Yildiz (2009)

For harvesting energy from mechanical vibration, electromagnetic, piezoelectric and electrostatic conversions are often applied. In order to test the feasibility and reliability of the different vibration energy sources, Marzencki (2005) [77] investigated these vibration energy

sources (electrostatic, electromagnetic, and piezoelectric) and compared the complexity, energy density, size, and challenges, as listed in Table 1.3.

According to Table 1.3, the electrostatic energy harvesting has low complexity of process flow and integrated size, compared with electromagnetic and piezoelectric. This indicates the electrostatic energy harvester is more compatible for microfabrication processes and can be easily integrated into the complicated systems. Therefore, electrostatic energy conversion is a promising solution for micro energy harvester.

Table 1.3 Comparison of vibration energy-harvesting techniques (Marzencki 2005)

	<i>Electrostatic</i>	<i>Electromagnetic</i>	<i>Piezoelectric</i>
Complexity of process flow	Low	Very high	High
Energy density	4 mJ cm <sup>-3</sup>	24.8 mJ cm <sup>-3</sup>	35.4 mJ cm <sup>-3</sup>
Current size	Integrated	Macro	Macro
Challenges	Very high voltage and need of adding charge source	Very low output voltages	Low output voltage

### 1.3.2 Electrostatic energy harvester

Electrostatic energy harvester operates based on a variable capacitor, generally in the form of a parallel plate capacitor, which can respond to the ambient vibration. In terms of whether involved with electret or not, the electrostatic energy harvesters can fall into two categories [78]: (a) electret-free; (b) electret-based. The former use conversion cycles made of charges and discharges of the capacitor, thus an external bias voltage is required. The latter employ electrets, allowing directly converting mechanical power into electricity [79-81].

Consider an electret-free converter, onto which a charge is introduced from an external power source. Assume the charging of the plates by a battery of voltage,  $V$ , generating equal but opposite charges on the plates,  $Q$ , subsequently leading to a storage of the charge when the voltage source is disconnected. The definition of capacitance in such a converter is,

$$C = \frac{Q}{V} \quad (1.3)$$

For a parallel-plate capacitor, the capacitance can be determined by,

$$C = \frac{\epsilon_r \epsilon_0 A}{d} \quad (1.4)$$

where  $\epsilon_r$  is the relative permittivity of the dielectret;  $\epsilon_0$  is electric constant,  $\epsilon_0 \approx 8.854 \times 10^{-12}$  F m<sup>-1</sup>;  $A$  is the overlap area of the parallel plates; and  $d$  is the separation between the two plates.

According to (4), any change of the parameters in the right side can cause capacitance variation. For a specific electrostatic converter, it is more convenient to realize based on change of either overlap area, or the gap between two plates. Roundy et al. [82] had specified the electrostatic energy harvesters into three basic configurations, as shown in Figure 5, namely, in-plane overlap varying, in-plane closing, and out-of-plane gap closing. Both the in-plane configurations create two variable interdigital capacitors with the capacitances 180° out

of phase [66]. Boisseau et al. [78] supplemented another basic configuration for electrostatic energy harvester, in-plane variable surface, either with full plate area or with patterned area (see figure 1.6).

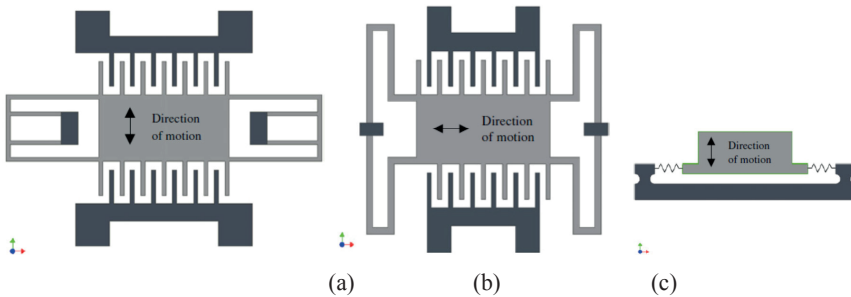


Figure 1.5 Basic configurations of electrostatic energy harvester (Reprinted from Ref. [82], Copyright (2002), with permission from ASME): (a) In-plane overlap varying; (b) In-plane gap closing; (c) Out-of-plane gap closing.

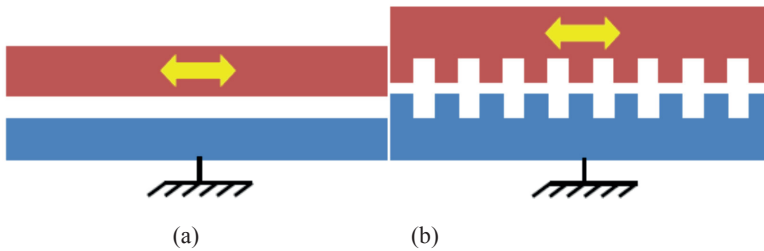


Figure 1.6 Another basic configuration of electrostatic energy harvester, in-plane variable surface by Boisseau et al. (2012): (a) full plate variable; (b) patterned surface variable.

It is also noted that all the forgoing basic configurations can be used for both electret-free and electret-based applications. There have been plenty of electrostatic energy harvesters during the last two decades, as reviewed by Beeby et al. (2006) [66], Harb (2011) [69] and Boisseau et al. [78].

Aside from the changes of overlap area and plate gap, the change of permittivity to realize electrostatic energy harvester has also been explored. Lallart et al. (2011) [83] proposed a vibration energy harvesting scheme using a two-layer configuration made of a high permittivity material and a low permittivity layer of variable thickness. Due to the significant change in the permittivity, the capacitance ratio variation is much larger than in the case of a single layer (whatever the permittivity of the latter), therefore allowing an increased efficiency and a significant energy gain, by a typical factor of 50.

Figure 1.7 illustrates several typical electrostatic energy harvesters, which employ spring-mass configuration.

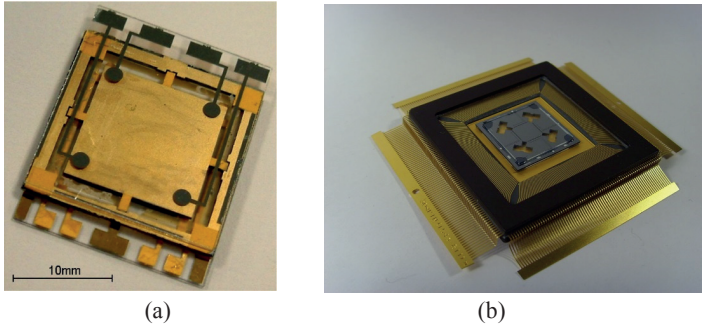


Figure 1.7 Typical electrostatic energy harvesters: (a) an electrostatic constant charge harvester for wideband operation from Imperial College, UK, Reprinted from Ref. [91], Copyright (2006), with kind permission from Springer Science and Business Media; (b) an electret-based converter for 3D energy harvesting from Furtwangen University, Germany, Reprinted from Ref. [84], Copyright (2011), with permission from SPIE.

According to Figure 1.5 and 1.6, the electrostatic energy harvester often comprises of mass-spring configuration. Moreover, most of such linear spring–mass systems are linear and are optimized to work at specific frequencies. A key design feature of such vibration-based harvesters was that they are optimally tuned to harvest energy within a narrow frequency band in the neighborhood of a natural frequency [85]. In order to improve the performance of harvesters operating in a wide band of frequency, researchers have been making many efforts. On the one hand, the self-tuning of the operation frequency has been proposed [86, 87], which are quite efficient but require additional power for an active conditioning circuit. On the other hand, adding nonlinearity into the structure by using non-linear springs [88] and involving end-stop effects [89] have been proposed, which are efficient for harvesting energy from stochastic vibrations. Moreover, Basset et al. (2014) [90] proposed a combination of end-stop effects and a strong biasing electrical field so that to realize a wideband operation of electrostatic energy harvester.

However, in some scenarios that require wideband response but low frequency excitation, the conventional spring suspensions have to be made more compliant to reduce the eigen frequency or even be discarded. Several efforts have been made to realize non-resonant energy harvesters. Miao et al. [91] reported a micro-generator that allowed the proof mass only to move during that portion of the motion cycle where acceleration is at maximum. Rolling [92, 93] or sliding [94-96] proof masses were also proposed for electrostatic energy harvesters.

Compared with that of the conventional solid spring-mass configuration, the inherent compliance of liquids suggests their promising applications as non-resonant electrostatic energy harvester, especially for low frequency excitation at several Hzs. This is the main motivation to develop a fluidic electrostatic energy harvester. In Chapter 2, an electrostatic energy harvester employing droplet and ionic marble rolling is to be investigated thoroughly.

## 1.4 Microfluidic two-phase flow

The microfluids of interest for chemistry and biotechnology application were rarely simple single-phase liquids [97]. Complex fluidic systems, such as nano-emulsion and micro-emulsion [98], play a very important role in drug delivery, food science, oil and dairy industries, and therefore require thorough study.

The emerging microfluidic cooling technique for high-flux electronics [39-41] demands better understanding of two-phase flow behaviors in microsystem devices. Besides, the two-phase flow phenomena in micro fuel cell also capture attentions.

In terms of the phase of working fluids involved, the microfluidic two-phase flow can be simply subdivided into two categories: microfluidic gas(vapor)-liquid flow and liquid-liquid flow.

### 1.4.1 Microfluidic gas-liquid flow

Microfluidic gas-liquid flow is often seen in droplet-based microfluidic systems for biomedical applications, e.g., cell stimulus and lysis [99]. To generate stable bubble train, the gas and liquid streams could be made to flow-in concurrently; but whilst the gas flows continuously, the liquid flow is pulsated, which results in a single-line segmented gas-liquid distribution in the microchannel [100]. Another method for the generation of monosized microbubbles dispersed in a liquid is called flow focusing [101], in which the gas was continuously supplied through a capillary tube to form a large bubble in the vicinity of a small orifice [102], as shown in Figure 1.8.

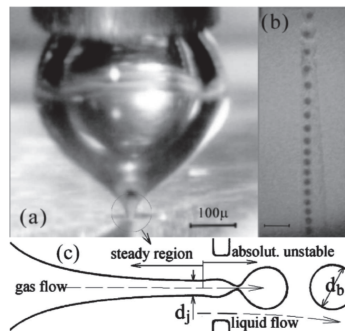


Figure 1.8 Flow focusing to generate monosized microbubbles [102], Copyright (2001) by The American Physical Society.

Typical microfluidic two-phase flow patterns, such as droplet-based microfluidics or the so-called “segmented flow”, which is essentially the elongated droplet flow, have been well

investigated. Plenty of early research on microfluidic gas/liquid flow have been reviewed in articles by Baroud and Willaime (2004) [103], Doku et al. (2005) [100], Shui et al. [104] and Zhao and Middelberg (2011) [105]. Here some recent advances in microfluidic gas/liquid two-phase flow are presented as below.

Tan et al. [106] conducted the experimental investigation on the mass transfer performance of segmented gas–liquid flows in T-junction microdispersion devices, in which the perpendicular shearing method was applied to generate the gas–liquid microflow. An *in situ* measuring method was developed, with which the overall mass transfer coefficient in the flowing stage could be determined by measuring the change of gas slug volume versus flowing distance.

Wang et al. [107] reported experimental investigations of gas-liquid two-phase flow regimes in micro-channels. Four distinctive flow patterns of slug flow, slug-annular flow, annular flow and parallel-stratified flow were observed. Novel empirical correlations for predicting flow pattern transitions during the steady gas-liquid flow in microchannels have been developed with the fluid properties and the wetting properties of microchannels.

Chong et al. [108] reported a method to control the bubble sized generated in a microfluidic flow-focusing configuration by induced acoustic streaming. It was found the induced acoustic streaming had significant effects on the formation process of gas bubbles. The gas-liquid oscillating interface acts as a pump that increases the gas flow rate and form a larger bubble. And the bubble size can be tuned repeatedly with response time on the order of seconds.

Yao et al. [109] reported flow and mass transfer of gas-liquid slug flow in a microchannel under elevated pressures up to 3.0 MPa with CO<sub>2</sub>-water system. It was found the ratio of the initial bubble length to the unit cell length was linear with the injection gas volume fraction under each pressure condition. The mass transfer coefficients were calculated with a unit cell model based on the dissolution rate of gas bubbles. And the increasing pressure leads to larger mass transfer coefficients, as well as higher amount of gas absorption during bubble formation.

Additional to the forgoing microfluidic gas-liquid two-phase flow, investigations on microfluidic two-phase (vapor-liquid) flow for high-flux electronic cooling have reported, such as, two-phase cooling for high power LED [40], DMF liquid using EWOD for hotspot cooling [110], etc. More related research can be found in the review articles by Hidrovo et al. (2006) [111] and Kandlikar et al. (2014) [41].

### **1.4.2 Microfluidic liquid-liquid flow**

When two immiscible liquids combined to flow in the microsystem, the microfluidic liquid-liquid flow happens, which is often seen in micro-reactor, micro-emulsion, and even double micro-emulsions [105].

Typically, the droplet-based microfluidic flow has been realized for some specific applications. The droplet formation can be realized in microfluidic T-junction geometries, flow-focusing, and co-flowing, as illustrated in Figure 1.9 [105]. Besides, more investigations on liquid-liquid microfluidic two-phase flow have been reported.

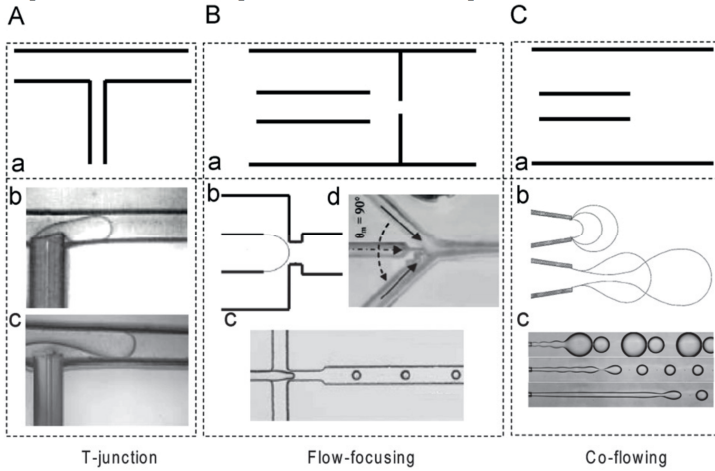


Figure 1.9 Geometric structures of microfluidic devices for droplet formation: (A) T-junction; (B) Flow-focusing; (C) Co-flowing. Reprinted from Ref. [105], Copyright (2013), with permission from Elsevier.

Visualized investigation on kerosene-water two-phase flow in PMMA microchannels was reported by Zhao et al. [112]. Typical oil-water flow patterns in microchannels, namely, slug flow, monodispersed droplets flow, droplet populations flow, parallel flow, as shown in Figure 1.10 (a); and a flow pattern map flow pattern transition lines in the microchannel as a function of the kerosene superficial Weber number and the water superficial Weber number was obtained, as Figure 1.10 (b).

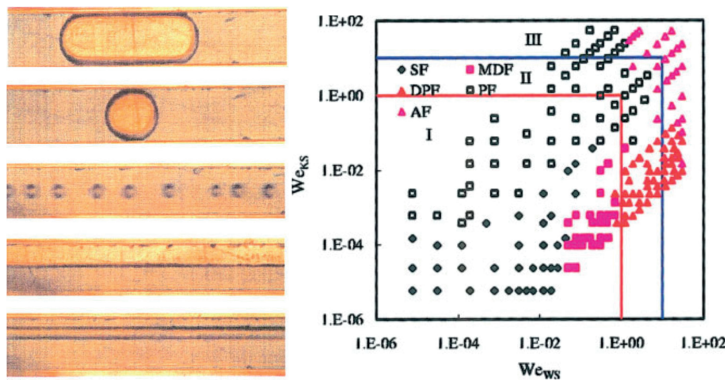


Figure 1.10 Oil-water two-phase flow pattern in microchannels: (a) typical flow patterns (from top to bottom), slug flow, monodispersed droplets flow, droplets populations flow, parallel flow; (b) flow pattern map. Reprinted from Ref. [112], Copyright (2006), with permission from John Wiley and Sons.



Monodispersed gas-in-oil-in-water (G/O/W) and gas-in-water-in-oil (G/W/O) double-emulsions in the same dual-coaxial microfluidic device were reported by Xu et al. [113]. The effects of three phase flow rates on the sizes of microbubbles and droplets and the number of the encapsulated microbubbles were systematically studied. Typical structures of the G/O/W double emulsions generated by adjusting the three phase flow rates are depicted in Figure 11.

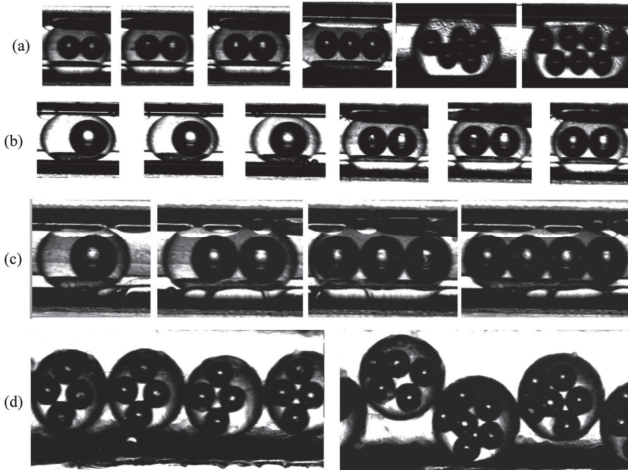


Figure 1.11 Different structures of the G/O/W double emulsions generated by adjusting the three phase flow rates. Reprinted from Ref. [113], Copyright (2012), with permission from Royal Society of Chemistry.

Recently, a microfluidic approach has been introduced to generate all-aqueous emulsions and jets based on these immiscible aqueous phases; due to their biocompatibility, these all-aqueous structures have shown great promises as templates for fabricating biomaterials. The progress on the immiscible aqueous phases with a focus on the fabrication and stabilization of all-aqueous structures in a multiphase microfluidic platform were reviewed by Song et al. (2013) [114]. Besides, future efforts needed from the perspectives of fluidic physics, materials engineering, and biology for fulfilling potential applications ranging from materials fabrication to biomedical engineering were also discussed.

With respect to the current status of microfluidic two-phase flow research, it is of great importance to have a good understanding of the flow pattern. Therefore, the promising sensing solution is required for microfluidic two-phase flow. Moreover, if it is compatible with the current microfabrication process, the solution shall be highly favorite for the researchers. In Chapter 3, a microfluidic flow pattern sensor is presented in details.

## 1.5 Main work of the thesis

With respect to the developments of interdigital capacitance, electrostatic energy harvesting and microfluidics two-phase flow, this thesis focus on the microfluidics sensing and transduction by use of interdigital capacitance. A droplet-based micro electrostatic energy

harvester and a microfluidic two-phase flow pattern sensor are demonstrated in this thesis. Both of them employ the interdigital capacitance.

The thesis are organized as following chapters. In chapter 2, droplet-based electrostatic energy harvester is presented including modeling, simulation, and experimental investigations. Both mercury droplet and ionic marbles are used to take place of the conventional spring-mass configuration. A considerable output has been achieved with this droplet-based electrostatic energy harvester. In Chapter 3, a microfluidic two-phase flow sensor is demonstrated, including analytical, simulation and experimental results. This microfluidic flow pattern sensor is capable of identify the typical flow patterns in microfluidic devices. Moreover, both velocity and size can be attracted from the acquired data. In Chapter 4, main conclusions are drawn for both droplet-based energy harvester and the microfluidic sensor. Besides, some prospects of the future work on the two prototypes of microfluidic transduction and sensing are addressed. In the last part, the publications related to the forgoing work are enclosed.

# Chapter 2

## Fluidic electrostatic energy harvester

In the application cases that involve with low frequency and wideband excitation, the conventional electrostatic energy harvester employing solid spring-mass may be not suitable. Inherently, fluids are more flexible and compliant, which suggests the emergence of fluidic electrostatic energy harvester for non-resonant applications.

This chapter comprises of detailed work of a fluidic electrostatic energy harvester, including overview of current fluidic electrostatic energy harvester, working principle, modelling, simulation, prototype fabrication, and test results.

### 2.1 Overview of fluidic electrostatic energy harvester

Several researches on fluidic electrostatic energy harvesters have been reported. Boland et al. (2005) [115] were the first to propose an electrostatic energy harvester employing fluids, which was a liquid-rotor electret power generator employing mercury droplets and air-filled gaps in a capacitor. The electret was made from a 25  $\mu\text{m}$ -thick Teflon<sup>TM</sup> fluorinated ethylene propylene (FEP) glued to an electrode. Krupenkin and Taylor (2011) [116] proposed a mechanical-to-electrical energy conversion method that was based on reverse electrowetting-on-dielectric (REWOD) phenomena. Actually, such REWOD principle is essentially no difference from the work of Boland et al., except for that the external bias was employed instead of the charged electret.

Later, Moon et al. (2013) [117] proposed a new method for electrical power generation by mechanically modulating the electrical double layers at the interfacial areas of a water bridge between two conducting plates. When the height of the water bridge was mechanically modulated, the electrical double layer capacitors formed on the two interfacial areas were continuously charged and discharged at different phases from each other, thus generating an AC electric current across the plates. This idea can be considered as a further development of the REWOD phenomena.

The concept of electrostatic energy harvester using encapsulated electrically conductive liquids was proposed by Löhndorf et al. (2008) [118], in which the liquid-gas interface within a chamber was changed freely in response to external excitation thus to change the capacitance. This concept was then demonstrated by Choi et al. (2012) [119], in which the conductive liquid functions as electrode. Similarly, Bu et al. (2012) [120] reported an electrostatic energy harvester encapsulating dielectric liquids instead of conductive liquids. Both of their work explored the possibility of involving fluids to change the capacitance.

As one unique category of conductive fluids, the room temperature ionic liquids (ILs) have properties which make them attractive fluids for energy harvesting, e.g., relatively high conductivity, non-volatility, and low toxicity (compared to mercury) [121]. Similar to the work of Moon et al., Kong et al. (2014) [122] demonstrated a vibration energy harvester using ILs instead of water, which can work without the need for an airtight space and operate at high or low temperatures. Additionally, IL marbles can be easily formed by rolling IL droplets in polytetrafluoroethylene (PTFE) powder [123], which turns each droplet into a completely non-wetting soft body [124].

Besides, some works on harvesting the kinetic energy of fluid flow by capacitance variation are reported. Borno et al. (2009) [125] presented a synthetic, microfabricated “leaf” to scavenge electric power from evaporative flow. Evaporation at the device produced flows with velocities up to 1.5 cm/s within etched microchannels; Gas-liquid interfaces inside the microchannels passed across an embedded capacitor at that velocity, generating 250 ms, 10 - 50 pF transient changes in capacitance. Yıldırım and Kūlah (2012) [126] reported energy harvesting technique by employing droplet-based microflow of two phases with different electrical permittivities, which resulted in a capacitance change across the microchannel. Experimental investigation was implemented in a 3 mm wide, 1 mm deep minichannels, and a power of 0.4 nW was harvested using a single electrode pair, with air and water as the two phases flowing at 1 ml/min.

More recently, electrostatic energy harvesters employing charged fluids have been reported. Miljkovic et al. (2014) [127] demonstrated a jumping-droplet electrostatic energy harvester, in which the charged droplets jump between superhydrophobic copper oxide and hydrophilic copper surfaces to create an electrostatic potential and generate power during formation of atmospheric dew. The microfabricated structured surfaces allow condensing coalesced droplets to spontaneously jump off the surface due to the conversion of excess surface energy into kinetic energy. Xie et al. (2014) [128] reported a microdroplet based electrostatic generator operating by an acceleration-deceleration cycle (‘ballistic’ conversion), in which water was accelerated by pumping it through a micropore to form a microjet breaking up into fast-moving charged droplets. Droplet kinetic energy was converted to electrical energy when the charged droplets decelerated in the electrical field that forms between membrane and target.

According to the review of available literature, the fluidic electrostatic energy harvesters can be represented by Figure 2.1. Except for direct accumulation of charged fluids, most of the fluidic electrostatic energy harvesters operate based on capacitance variation, which is realized either by varying relative permittivity, such as, Boland et al. (2005) [115], Krupenkin and Taylor (2011) [116], and Yıldırım et al. (2012) [126], or by changing the distance of the electrode plates, e.g., Löhndorf et al. (2008) [118], Choi et al. (2012) [119], Bu et al. (2012) [120], and Kong et al. (2014) [2014]. The fluids employed in can be either conductive or dielectric; and the electrodes used can be in parallel-plane form, or flexible conductive liquids. Moreover, the fluidic electrostatic energy harvester can be either by externally biased [116, 117] or with embedded electret [115], which is similar to the conventional spring-mass

electrostatic energy harvester.

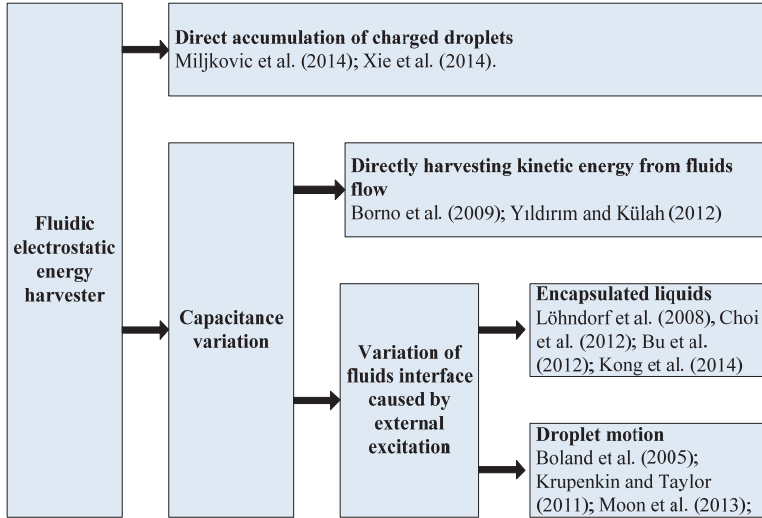


Figure 2.1 Status of fluidic electrostatic energy harvester research.

In this chapter, we propose and demonstrate a novel electrostatic energy harvester, which employs conductive droplets and IL marbles rolling across the coplanar electrodes covered by a thin charged electret. This fluidic energy harvester is more suitable for low frequency reciprocating motion, such as body motion, etc.

## 2.2 Working principle and modeling

### 2.2.1 Working principle

The fluidic electrostatic energy harvester operates on a variable capacitance caused by the droplet/marble rolling across the electrodes, as shown in Figure 2.2. Thin electrodes are patterned on a glass wafer and coated by an electret film. Additional capacitance can be induced when a conductive droplet rolls across the electret-film coated electrodes. When the droplet-electrode overlap area  $A_i$  ( $i=1$  or  $2$ , Figure 2.2b) has linear dimensions much greater than the film thickness  $d$ , the droplet-electrode capacitance at time  $t$  is simply estimated by

$$C_{\text{var},i} = \varepsilon A_i(t)/d \quad (2.1)$$

where  $\varepsilon$  is the permittivity of the insulating film. In terms of (2.1), the capacitance can be devised theoretically as big as possible by making the film thin enough. Practically, the thickness of the film is restrained by the insulation requirement; it has to be thick enough to secure the insulation between the droplets and the electrodes.

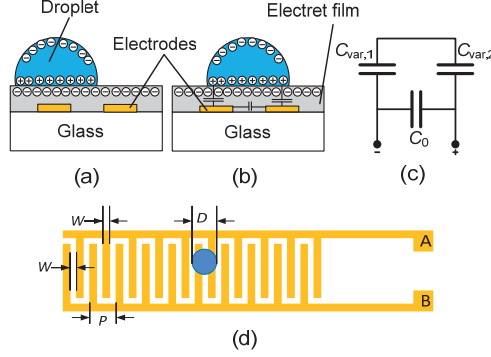


Figure 2.2 Schematics of the working principle: (a) droplet covers one electrode; (b) droplet covers two electrodes; (c) equivalent capacitor network; (Reprinted with permission from [129]. Copyright 2012, American Institute of Physics.) (d) configuration of interdigital electrodes with contact pads A and B for external connection.

The minimum and maximum capacitances occur when the droplet is covering one electrode (Figure 2.2a) and the overlap between two electrodes (Figure 2.2b), respectively. When the droplet does not overlap with an electrode, like for the rightmost electrode in Figure 2.2a, the droplet-electrode capacitance is small and entirely given by fringing field effects. The resultant variable electrode-electrode capacitance can be modeled as shown in Figure 2.2c and is

$$C_{var} = C_{var,1} \cdot C_{var,2} / (C_{var,1} + C_{var,2}) \quad (2.2)$$

where the maximum capacitance occurs when  $C_{var,1} = C_{var,2}$ . The total capacitance decreases to a minimum value when either of the capacitances goes to a small value. In addition to the variable capacitance, there will be a variable open-circuit voltage on the port due to the charges in the electret film. The detail of the interdigital electrodes (IDEs) is depicted in Figure 2.2d, in which  $P$  is the distance between the two adjacent fingers on the same arm of IDEs. Electrodes and gaps have the same width  $W$  so that  $P = 4W$ .

## 2.2.2 Modeling

In order to analyze the output of the device, we use the simple harvester model shown at the top of Figure. 2.3. The effect of the charges embedded inside the electret film is a built-in potential that can be represented as an ideal voltage source  $V_e$ . This voltage is then the open-circuit voltage of the equivalent circuit. The total capacitance is comprised of the nominal capacitance between the IDEs and the capacitance variation induced by the sliding or rolling droplet as expressed in (2.3). It is noted that the additional external bias voltage  $V_b$  indicated in Figure. 2.3 was only applicable for the quantitative investigation of the embedded charges described in 2.4.2. In all the other testing cases,  $V_b$  was set to zero.

The dynamic behavior of the equivalent circuit including the external bias voltage can be described by

$$\dot{Q} + Q(t)/(R_L C_{tot}) = -(V_e + V_b)/R_L \quad (2.3)$$

where  $Q$  is the charge on the variable capacitance; and  $R_L$  is the load resistor.

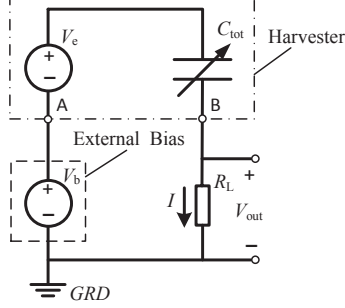


Figure 2.3 Electric circuit representation of the harvester and external components.

According to Figure. 2.3, the output voltage  $V_{out}$  varies due to changes in the variable capacitance or the open-circuit voltage caused by the droplet motion. As can be seen that the smallest time scale related to droplet motion is on the order of 10ms, while the electrical time constant is on the order of 0.1ms. Therefore, the electrical part quickly adjusts to changes in the mechanical part and it is reasonable to assume that the charge closely follows its short-circuit value. That is,

$$Q \approx Q_{SC} = -(V_e + V_b)C_{tot} \quad (2.4)$$

and (2.3) simplifies to

$$\dot{Q} = -d[(V_e + V_b)C_{tot}]/dt \quad (2.5)$$

Further simplifications can be made if we assume that the droplet shape does not change with droplet velocity, angular momentum, acceleration or higher derivatives, and is independent of the pre-history. In this case  $Q_{SC}$  is only dependent on droplet position  $x$  and the output voltage can be estimated by

$$V_{out} = R_L I \approx -R_L \dot{Q}_{SC} = -R_L \frac{dQ_{SC}}{dt} = -R_L v \frac{dQ_{SC}}{dx} \quad (2.6)$$

The output voltage, position, and velocity  $v$  can be determined as functions of time from measurement results. Therefore, (2.6) can be used to investigate the details of the working principle of the energy harvester.

## 2.3 Simulation

### 2.3.1 Physical model

The droplet based electrostatic energy harvester (as shown in Figure 2.4a) can be physically

modelled by a simple equivalent circuit (Figure 2.4b). The embedded charges inside the thin insulation film give rise to the voltage source  $V_e$ , while the resultant capacitance from the two terminals of the interdigital electrodes involving the conductive droplet can be simplified as a variable capacitance. Thus the relation between the embedded potential and the terminal potential can be expressed by,

$$V_{\text{out}}(x) = V_e(x) + Q(x)/C(x) \quad (2.7)$$

As the droplet moves across the thin film, the resultant capacitance varies in pace with the droplet displacement with respect to IDE fingers.

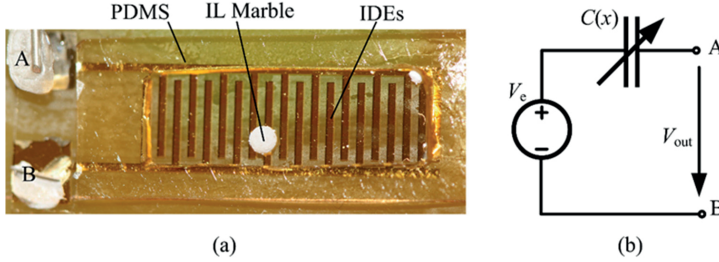


Figure 2.4 Droplet-based electrostatic energy harvester. (a) Optical photo of prototype; (b) Equivalent circuit characterizing the energy harvester.

### 2.3.2 Simplifying assumptions

The device has greatly varying length scales within it, posing serious challenges for FEA meshing, i.e., 100nm metal film thickness, micrometre scale film thickness, millimetre scale of droplet/electrode pattern and centimetre scale device dimensions. With the technical difficulties of meshing considered, the following assumptions were applied in the model to make FEA achievable:

- the IDE finger is treated as 2D structure with zero thickness;
- the variation of droplet profile due to the droplet dynamics or electrostatic forces has been neglected;
- and the droplet is simplified as a spherical cap with a circle contact area on the dielectric film.

As the thickness of IDE finger is rather small compared with the thickness of insulation film, the 2D model can reduce the meshing difficulty but without losing the transducing feature of IDEs. And the simplifications on the droplet profile actually characterize a static droplet, without addressing the dynamic behaviour. Therefore, these assumptions are reasonable. In addition, the charge distribution in the thin film is not known. As a first investigation, we therefore consider a uniform space charge density and investigate its consequences.



### 2.3.3 Simulation domain and procedure

The simulation domain is depicted in Figure 2.5. The droplet was treated as a conductor and PTFE was used as the insulation film. The detailed geometrical parameters are listed in Table 1.

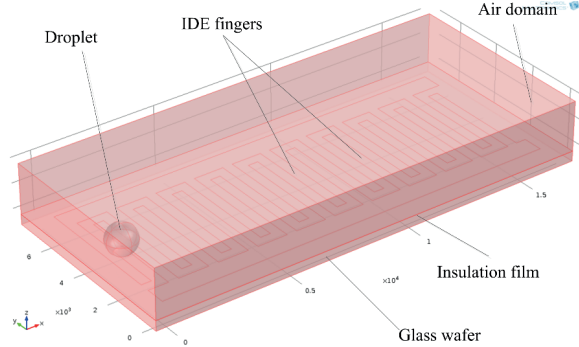


Figure 2.5 Schematic drawing of simulation domain.

Table 2.1 Parameters of the simulation domain.

Parameters	Unit	Value
Finger width of IDE	$\mu\text{m}$	400
Finger gap of IDE	$\mu\text{m}$	400
Number of finger pair	–	10
Droplet size	$\mu\text{m}$	1200
Insulation film thickness	$\mu\text{m}$	2
Glass substrate thickness	$\mu\text{m}$	400
Thickness of air domain	$\mu\text{m}$	2000

The simulation was conducted by the MEMS module of the commercial software COMSOL Ver. 4.3. Charge conservation was set for the whole simulation domain with 0-V boundary on the outer surface of the domain and also on the bottom surface of the glass substrate so as to match with practical testing where the device was placed on a conducting surface.

In order to obtain the capacitance variation with respect to the droplet displacement, a particular fine mesh was generated for IDE fingers and the thin film, as illustrated in Figure 2.6. As an aid in the difficult meshing of the thin film structure, virtual surfaces were used to control the mesh generation.

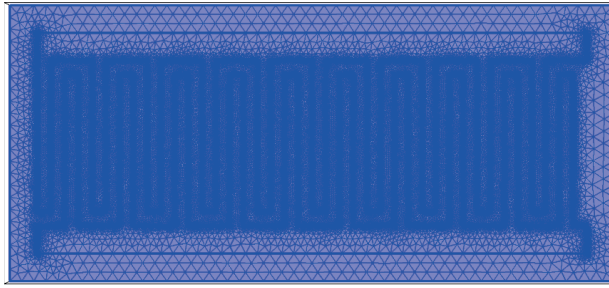


Figure 2.6 Meshing of the IDE fingers and thin insulation film (top view).

While the droplet moves along the central axis (x-direction) of the simulation domain, the capacitance was determined by applying 1.0V and 0V on the two terminals (A and B), respectively. The variation of the open-circuit potential of the prototype was checked by setting terminal A to zero charge while keeping terminal B grounded. Finally, the short-circuit charges on each electrode were checked by setting both to ground. A uniform space charge density was arbitrarily set at  $-1.0 \text{ C/m}^3$  for the insulation film. This is meaningful as the electrostatics is linear and only a scaling is necessary to correct the result to another value of embedded charge.

## 2.4 Prototype fabrication and test

### 2.4.1 Microfabrication of the prototype

A prototype of the fluidic energy harvester has been fabricated with the process flow illustrated in Figure. 2.7. The gold IDEs with thickness 100 nm were patterned on a 4-inch Pyrex 7740 glass wafer by sputtering and wet etching, see from Figure 2.7a to 2.6c. Then a 2- $\mu\text{m}$  thick PTFE film was deposited to coat the patterned IDEs by radio frequency (RF) magnetron sputtering (Figure 2.7d).

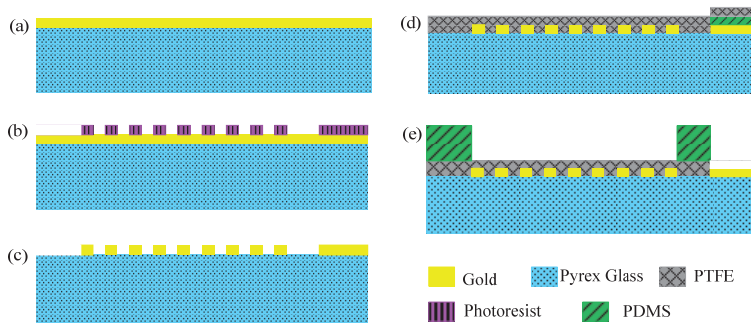


Figure 2.7 Schematic drawing of microfabrication process, not to scale: (a) Gold deposition; (b) Patterning IDEs; (c) Wet etching; (d) Magnetron RF sputtering; (e) PDMS baffle wall adhesion.

Being ionized by RF power, the Argon ions from the plasmas strike the PTFE target to deposit polymer molecules onto the substrate during the sputtering procedure. Meanwhile, the electrons also accumulate in the thin electret film together with the PTFE particles. With an electrostatic voltmeter (Isoprobe, Model 279), we verified the presence of a considerable charge accumulation in the thin film after the sputtering process. The average surface potential above the RF sputtered PTFE film was measured at -16V (after 14 months) with the device resting on a grounded surface.

As discussed previously, the thickness of the electret film is one of the key parameters affecting the resulting capacitance. Thus the thickness of PTFE film was well controlled by repeated deposition of the thin layers, so as to compromise between a reliable insulation and a considerable capacitance variation. Additionally, the area of the contact pads in IDEs was masked by a polydimethylsiloxane (PDMS) slice to protect from deposition of PTFE.

To prevent the droplet from sliding out of the electrode area, a solid baffle made of PDMS was adhered around the electrode area on the thin electret film, as shown in Figure 2.7e.

### 2.4.2 Test setup

A device under test is shown in Figure 2.8. For convenience of testing, the circuit was arranged on a printed circuit board (PCB), onto which the droplet energy harvester prototype was glued, see Figure 2.8a. The contact pads of the IDE, marked A and B, were connected to the load resistor and external bias voltage in series as previously shown in Figure 2.2.

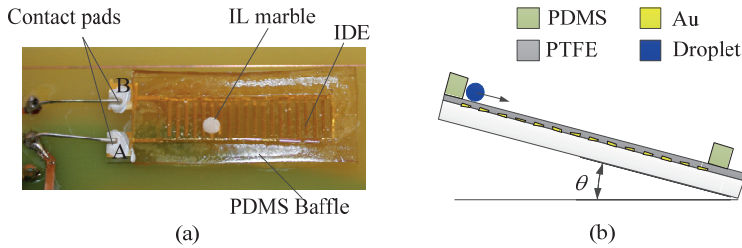


Figure 2.8 Device under test: (a) Photo of prototype device mounted on a PCB; (b) Test condition.

During the tests, we let a conductive droplet travel across the IDEs on the PTFE film, from top to bottom of the slope, of which the inclination angle is depicted in Figure 2.8b. Several inclination angles  $\theta$  were chosen to make the droplet roll with a specific acceleration.

The output voltage of the test circuit shown in Figure 2.8 was buffered through a BURR-BROWN<sup>®</sup> OPA137 OP-AMP and recorded by LabView v9.0.1 with a NI-USB-6211 DAQ connected to a laptop. The sampling rate was 24kHz. The value of load resistor  $R_L$  was not optimized. As the instantaneous output power is given by  $P_{out}(t) = V_{out}^2/R_L$ , the accumulated electric energy generated during a droplet traversal of the IDE can be evaluated as,

$$E_{\text{output}} = \int_{t_0}^t P_{\text{out}}(t) dt. \quad (2.8)$$

In order to quantitatively determine the potential caused by the embedded charges inside the PTFE film, we first devised and performed a special test: We used the direct series bias  $V_b$  as shown in Figure 2.3 and let a metal ball (2 mm in diameter) roll down the electret film. The output voltage was recorded and analyzed. Metal balls were chosen for this particular test because they were easier to handle in a great number of repeated tests. The bias voltage ranged from -400V to 400V.

To investigate the output performance of the prototype, all subsequent tests were performed using either a mercury droplet or an IL marble as a proof mass.

The IL marble was prepared by letting a 1- $\mu\text{l}$  droplet of 1-ethyl-3-methylimidazolium tetrafluoroborate (EMIM BF<sub>4</sub>) roll in PTFE powder (1 micron in particle diameter, Sigma-Aldrich<sup>TM</sup>), so that the droplet surface was coated with a layer of particles, as shown in Figure 2.9a. Without disturbance, this marble can keep a stable ball-shape for a long time under ambient conditions. In Figure 2.9, pictures of an IL marble and a mercury droplet under a microscope are also shown.

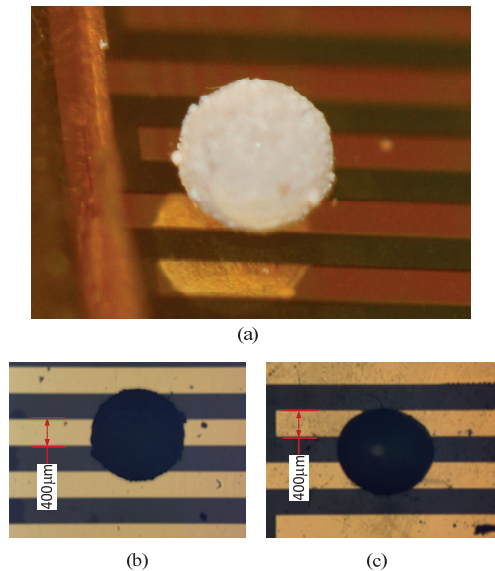


Figure 2.9 Liquid proof mass on interdigital electrode pattern: (a) photo of IL marble with a diameter of 1.2 mm on 500  $\mu\text{m}$ -wide electrode; (b) IL marble with a diameter of 1.2 mm on 400  $\mu\text{m}$ -wide electrode; (c) mercury droplet with a diameter of 1.2mm on 400  $\mu\text{m}$ -wide electrode under an optic microscope.

## 2.5 Results

### 2.5.1 Simulation results

#### 1. Capacitance variation and open-circuit voltage

Figure 2.10 and Figure 2.11 plot the variations of the capacitance and open-circuit voltage with respect to the droplet position, respectively. It is noted that the maximum values occur at the positions where the droplet is right in the middle of the two adjacent fingers (gap center) while the minimums are corresponding to the positions where the droplet are sitting right on the top of one finger (finger center). Moreover, the capacitance varies sharply as the droplet moves from the gap center towards the finger centre, which can explain why the narrowly peaked output voltage appears in the test results [129].

According to Figure 2.10, the range of capacitance variation in the energy harvester is not so impressive for a droplet having a diameter of 1.20 mm, less than 0.2 pF. For the real prototype, the thickness of insulation layer was smaller, down towards 1.0 micron, thus the capacitance variation is larger.

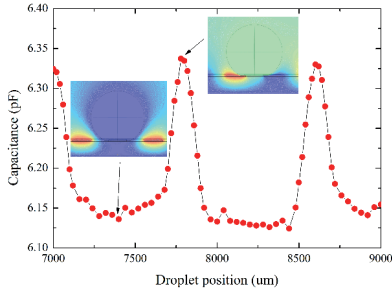


Figure 2.10 Capacitance variation with droplet position.

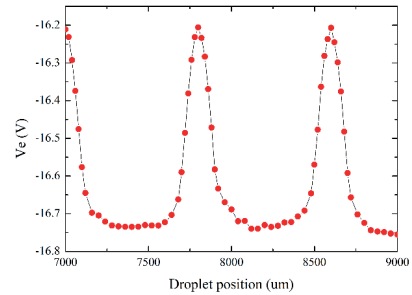


Figure 2.11 Open-circuit potential variation with droplet position

#### 2. Charge variation on the grounded electrodes

Figure 2.12 plots the charge distribution on the two terminals under grounded condition with the droplet moving within one period (four times of finger width) of IDE configuration. Due to computational errors, there are considerable fluctuations in the result. The reason for the small variations, in the third decimal, is cancellation which can be verified by calculating short-circuit charge as the product of the results in figures 2.10 and 2.11 and gives a variation that drowns in numerical error (not shown). The peak in the open circuit potential of figure 2.10 is a notch in its magnitude that nearly cancels the corresponding peak in the capacitance. However, figure 2.12 still indicates some tendency of the charge variation with respect to the droplet position: the charge variations on the two terminals alternate and reach nearly the

same value at the positions when the droplet is at the gap centre. This is also where the change is largest which would give peaks in the derivative of the short-circuit charge that alternate with the period shown in the experiments. Therefore, a uniform charge distribution in the film seems to be able to qualitatively account for the observed behaviour, but numerical accuracy needs improvement to make a quantitative test.

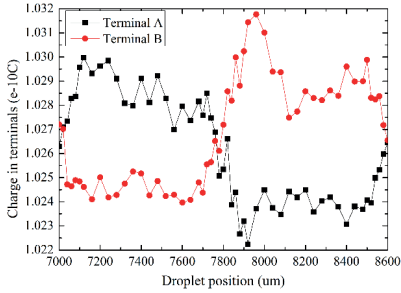


Figure 2.12 Charges on the grounded electrodes.

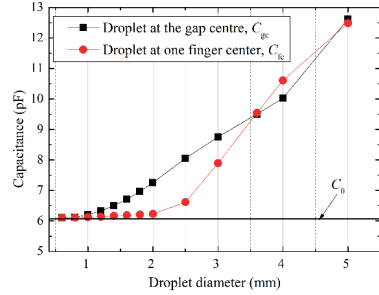


Figure 2.13 Influence of droplet size on the capacitance variation.

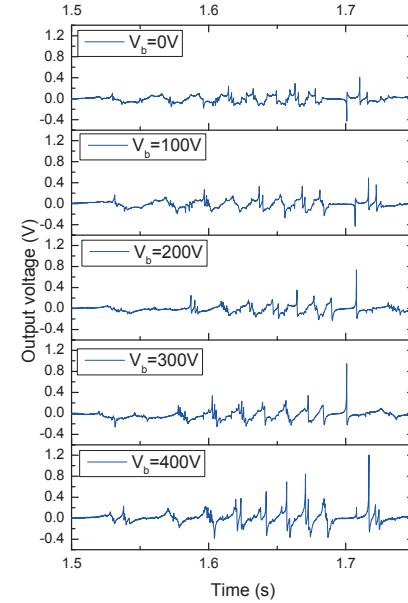
### 3. Influence of droplet size on the capacitance variation

The influence of droplet size upon the capacitance is plotted in Figure 2.13, in which the droplets hold a constant contact angle of  $60^\circ$  with both positions at gap centre (gc) and finger centre (fc). It is clear that for the IDE with finger/gap width of  $400\mu\text{m}$  ( $C_0=6.09\text{pF}$ ), the total capacitance variation ( $\Delta C=C_{gc}-C_{fc}$ ) increases rapidly with the droplet size, and has a maximum of  $1.4\text{pF}$  for a droplet size of  $2.5\text{mm}$ . The variation drops as the droplet size keep increasing, even turns to negative when the droplet covers more than one pair of fingers. This indicates that the droplet size should be matched well to the IDE pitch and could favourably have been considerable larger than what was used in the previous experiments. The finding explains why a bigger droplet gave larger output from the test [Paper 3].

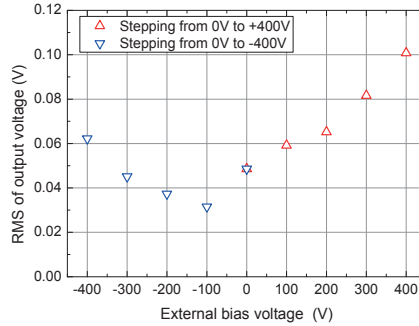
## 2.5.2 Test results

### 1. The embedded charges inside the PTFE film

Figure. 2.14 shows the output-voltage waveforms for different bias voltages. The general trend indicated by this data set appears to be that the higher the bias voltage is, the higher the peak output voltage is. However, the waveforms are somewhat irregular, in particular with respect to the voltage peaks, and it is hard to determine by inspection if there is any significant difference between e.g. the 0-V and 100-V traces. We therefore use the root mean square (RMS) voltage instead of peak voltage to determine the effect of bias.



(a)



(b)

Figure 2.14 Output voltage with various external bias voltages utilizing metal ball: (a) Transient output voltage; (b) RMS output voltage.

Figure 2.14b depicts the RMS output voltage versus the external bias voltage. The measurements were made by first stepping the voltage from 0V up to 400V, then from 0V down to -400V. The two sequences are distinguished by different markers in the figure. That the RMS output voltages with 0-V bias coincide in the two sequences shows that residual charging effects are not responsible for the observed asymmetry with respect to voltage. A minimum RMS  $V_{\text{out}}$  of about 0.03V is found at about -100-V bias voltage. If  $V_e$  had been constant in (2.5), we should have had zero output at the minimum. Instead, we get a minimum RMS output voltage of 0.03V which is comparable to the change in output seen when varying

the bias between  $-400\text{V}$  and  $+200\text{V}$ . Therefore  $V_e$  must have a considerable variation as the droplet moves and its value must be around  $100\text{V}$  in an average sense. Furthermore, it is clear from (2.5) and (2.6) that the RMS output voltage would not have had any bias dependence unless the capacitance too changes with droplet motion.

## 2. Typical output performance

Figure 2.15 illustrates dynamic output voltage across the load resistor (insets) and the corresponding accumulated output energy (2.8), with mercury droplet and IL marble rolling across the electret-film area in the prototype. The electrode finger width is  $W=500\mu\text{m}$ .

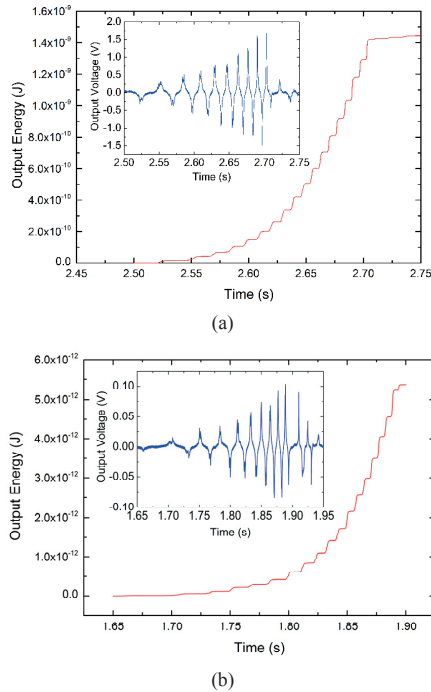


Figure 2.15 Accumulated output energy vs. time; Insets show corresponding instantaneous voltage: (a) mercury droplet,  $D=1.2\text{mm}$ , inclination angle  $\theta=20^\circ$ ; (b) IL marble,  $D=1.2\text{mm}$ , inclination angle  $\theta=15^\circ$ .

In terms of the instantaneous output voltage in Figure. 2.15, the positive peaks and negative peaks appear alternately as the droplet/marble travels across each pair of fingers of the IDEs. The maximum output voltage and output power occur when the droplet has reached its maximum velocity at the far end of the electret film.

For a mercury droplet with diameter  $1.2\text{mm}$ , a maximum instantaneous output power was recorded at around  $0.18\mu\text{W}$  while the mean output power for one cycle was  $7.78\text{nW}$  and the output energy is  $1.5\text{ nJ}$  for one traversal, which we can think of as representative of a half



cycle if periodically tilting the device.

According to Figure 2.15b, the output performance of the prototype with IL marble was weaker as its output voltage is much lower, i.e. by less than 1/10, which is smaller than that can reasonably be explained by the larger inclination angle for the mercury droplet. There are slight differences in the waveforms of the instantaneous output voltage between the two cases.

Thus the ratio of their accumulated output energies, calculated by integration, does not quite correspond to the ratio of their peak voltages.

### 3. Dynamic behavior of the rolling droplet/marble

We now analyze the droplet dynamics semi-empirically with regard to (2.6). For a droplet with big contact angle, such as the mercury droplet and IL marble, at low velocities, the contact angle variation with velocity can be neglected [130]. This conclusion is valid when the Reynolds number  $Re=UD/\nu < 8150$ , where  $U$  is the velocity and  $\nu$  is the kinematic viscosity of the droplet or liquid marble. For all test cases in this work, the maximum Re number is around 1800. Hence, as a first approximation, it is reasonable to neglect the contact variation of the droplet in analyzing the measured data and assume negligible deformation of the droplet with increasing velocity. Moreover, the envelope of the output voltage appears approximately linearly increasing with time in Figure. 7. From (2.6) and the assumption of no velocity-dependent deformation, we then conclude that the droplet acceleration appears to be approximately constant. Hence, the displacement of the droplet during rolling is

$$x = a(t - t_0)^2 / 2 \quad (2.9)$$

in which both the acceleration  $a$  and initial time point  $t_0$  can be obtained by a least squares fit (LSF).

As the distance between adjacent electrode fingers of the IDE is uniform, the time instants  $t_n$  with  $n=1, 2, \dots, 9$  when the droplet passes the  $n$ -th finger of one electrode can be recognized from the time-voltage data. And each pair of consecutive time instants corresponds to the same travel length, i.e.  $x(t_{n+1}) - x(t_n) = P$ . Hence, a sequence of time instants for the droplet passing each electrode finger can be deduced from the data sampling. We chose the zero crossings on the trailing edges of the voltage waveform as the time instants. Then, LSF was performed for the time sequence by minimizing

$$\sum_n [(\bar{t}_n - t_0) \Delta t_n - H]^2 \quad (2.10)$$

where  $\bar{t}_n = (t_{n+1} + t_n) / 2$ ,  $\Delta t_n = t_{n+1} - t_n$  and  $H = P/a$ .

A typical fitted result for the mercury droplet together with the measured data is plotted in Figure 2.16. It shows a reasonable agreement between the fitted and measured points except, perhaps the first point. This indicates that the rolling droplet actually behaves quite like “free-fall” motion. The deviation at the first point can be due to change in friction when the droplet goes from the static to the dynamic state. In Figure 2.17, a similar analysis for the IL marble is plotted.

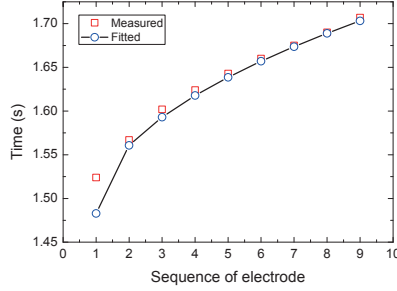


Figure 2.16 Dynamic behavior of the mercury droplet rolling ( $D=1.2\text{mm}$ , inclination angle  $\theta=15^\circ$ ).

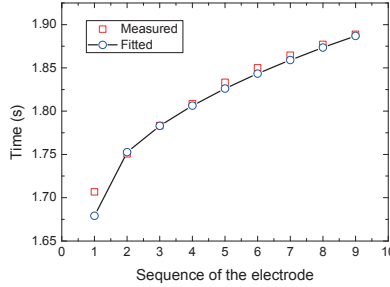


Figure 2.17 Dynamic behavior of the IL marble rolling ( $D=1.2\text{mm}$ , inclination angle  $\theta=15^\circ$ ).

We can compare the acceleration from the LSF to the ideal one calculated from gravity and the inclination angle as listed in Table 1 for both mercury droplets and IL marbles. It shows that the fitted acceleration from LSF is only a little bit lower than the ideal quantity (without any friction); and the deviation from the ideal quantity is approximately constant. The damping effects seem to be independent of the inclination angle according to the test results in Table 1, i.e. like Coulomb damping.

Table 2.2 Comparison of acceleration from LSF vs. ideal value (Unit:  $\text{m/s}^2$ )

	Inclination angle $\theta$ ( $^\circ$ )	From LSF ( $a_{\text{LSF}}=P/H$ )	Frictionless ( $a_{\text{ideal}}=g\sin\theta$ )	$\Delta a$ ( $a_{\text{LSF}} - a_{\text{ideal}}$ )
Mercury droplet	12	1.9032	2.0375	-0.1343
	15	2.4032	2.5364	-0.1332
	20	3.2215	3.3518	-0.1303
	22	3.5424	3.6711	-0.1287
IL marbles	12	1.8548	2.0375	-0.1827
	15	2.3551	2.5364	-0.1813

Additionally, according to the fitted acceleration data, the damping effect for the marble appears a little higher than that for the mercury droplets.

The energy spectrum of the output voltage, estimated as the squared magnitude of the discrete Fourier transform of the sampled  $V_{out}$ , is shown in Figure 2.18 for a rolling mercury droplet. It is clear that the most of the spectral weight falls into the frequency range below 100Hz, indicating that the shortest time scale of droplet motion is around 10ms. This time scale is much longer than the electrical time constant  $R_L C_{tot} \approx 0.08\text{ms}$  based on an estimated  $C_{tot} \approx 5\text{pF}$ . Hence, the short-circuit-charge assumption in (2.4) is reasonable.

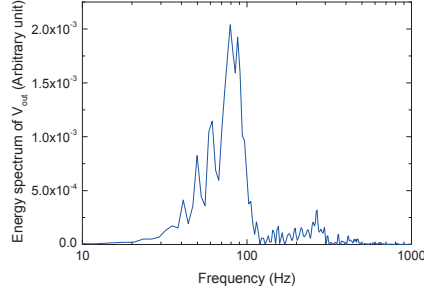


Figure 2.18 Spectrum of the output voltage with a mercury droplet ( $D=1.2\text{mm}$ , inclination angle  $\theta=15^\circ$ )

With the parameters determined by LSF, the output voltage could be calculated from (2.6) if we knew the short circuit charge  $Q_{sc}$ . Figure. 2.19 illustrates a model calculation based on the naive assumption of a simple harmonic waveform with period  $P$  for  $Q_{sc}$  as a function of position only, together with the measured results. The simplified model roughly matches the envelope and period of the output voltage, but deviates considerably w.r.t. the detailed waveform of the measured results. Therefore, even if  $Q_{sc}$  is a function of  $x$  only, it must contain considerable higher harmonics. We also notice that the deviations are larger at the early stage of droplet rolling in Figure 2.18. This suggests that droplet behavior deviate more from the “free-fall” behavior during the early stage when the droplet starts to roll from the static state, as we have observed in Figure 2.16.

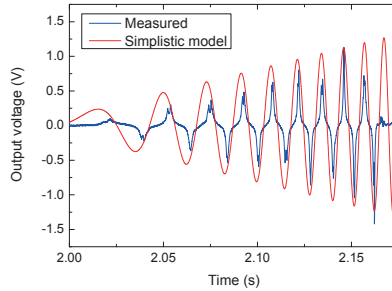


Figure 2.19 Comparison of the modeling plots with the test data (Mercury droplet,  $D=1.0\text{mm}$ , inclination angle  $\theta=15^\circ$ )

As the initial time point  $t_0$  can also be obtained from LSF, the assumption of  $Q_{sc}$  being only a function of  $x$ , can then be checked. The  $dQ_{sc}/dx$  can be determined from measured quantities by rearranging (2.6) into  $dQ_{sc}/dx = -V_{out}/(RLV)$ . The  $dQ_{sc}/dx$  versus displacement  $x$  is plotted in Figure. 2.20. Away from the ends, it shows a constant period of variation with approximately the same strongly peaked form within each period. The differences between the peak values can be caused by the charge nonuniformity as well as surface irregularity in the electret film.

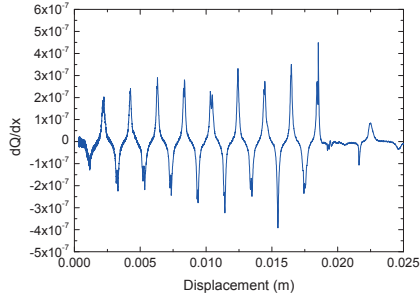


Figure 2.20 The charge variation rate with respect to displacement, based on the test data with mercury droplet,  $D=1.0\text{mm}$ , inclination angle  $\theta=15^\circ$ .

#### 4. Factors affecting on the output performance

It is obvious that parameters such as the dimension of the droplet, electrode dimension, acceleration of the droplet may affect the output characteristics of the device. Here we give some examples to illustrate the variation.

Figure. 2.21 shows the output energy of the prototype with different mercury droplet dimensions (prototype electrode width  $W=500\mu\text{m}$ ). As described in section II, the capacitance variation depends on several parameters, such as, thickness of the film, overlap area between the droplet and electrode, etc. For a given electrode width  $W$ , a larger dimension of the droplet means a larger overlap area, thus resulting in a larger capacitance variation. According to Figure. 13, the droplet with the larger dimension ( $D=1.2\text{mm}$ ) has better output performance compared with smaller droplet ( $D=1.0\text{mm}$ ) for the given electrode configuration.

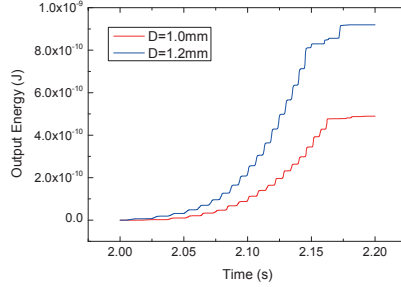


Figure 2.21 Accumulated output energy versus time for different dimensions of mercury droplet with inclination angle  $\theta=15^\circ$ .

However, the droplet dimension should somehow match with the configuration of the IDEs, i.e., the width and gap of the electrode fingers. Consider the situation in Figure. 1b when one droplet covers only one pair of electrodes given that the electrode width is equal to the electrode gap. The droplet size should be at least as big as the electrode gap in order to cover part of one electrode couple. Meanwhile, the droplet size should be less than  $4W$ , otherwise the droplet could cover more than one electrode couple. Therefore, the optimal droplet dimension  $D$  is expected in the range  $W \leq D \leq 4W$ . How the detailed matching between the two parameters should be optimized to give rise to maximum capacitance variation requires more investigations.

Figure 2.22 illustrates the output energy of the prototype obtained from different accelerations with the same mercury droplet ( $D=1.0\text{mm}$ ). The inclination angle was changed to give different output. For convenience of comparison, the time scales have been aligned. The small spread between the 3 data sets for each inclination angle indicates the repeatability of the test. In terms of (2.6), the output-voltage envelope is in proportion to the instantaneous velocity. Therefore, the larger acceleration leads to higher accumulated output energy when the droplet travels across the fingers of IDE. Denoting the accelerations, final velocities and time of rolling for the different inclination angles by  $a_1$ ,  $a_2$  ( $a_1 > a_2$ ),  $v_1$ ,  $v_2$ ,  $T_1$  and  $T_2$ , respectively, the motion at constant acceleration yields  $a_1/a_2 = (T_2/T_1)^2$  and  $v_1/v_2 = T_2/T_1$ . As can be further verified from Figure.14, for two different inclination angles,  $(T_2/T_1)^2$  roughly matches with the ideal ratio  $a_1/a_2 = \sin \theta_1 / \sin \theta_2$ .

If the load resistance had been high enough to make the electric time constant much larger than the mechanical time scale, the output power would instead have been independent of the acceleration and proportional to the mean-square open-circuit voltage. Figure. 14 therefore confirms that the device operate in the velocity-sensitive regime described by (2.6).

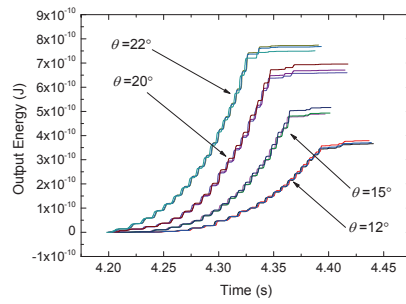


Figure 2.22 Accumulated output energy versus time for different inclination angles ( $D=1.0\text{mm}$ ).

More discussion on the performance of this fluidic electrostatic energy harvester can be found in **Paper 2** and **Paper 3** attached in Chapter 5.

## Chapter 3

# Microfluidic two-phase flow pattern sensor

As two immiscible fluids are brought to contact in microchannels, microfluidic two-phase flow occurs. Microfluidic two-phase flow has been seen very often in microsystem devices, lab-on-a-chips [131], micro chemical systems [105], micro reactors [7, 100], and micro fuel cells [132], etc. Compared with single-phase flow, two-phase flow increases the transfer of heat, mass and momentum, meantime multiplying the complexity of microfluidic flow consequently. It has been recognized that when the channel size shrinks from conventional scale to micro scale, the ratio of the surface area to the volume is increased; and the microfluidic flow patterns are very much influenced by roughness, shape and wettability of the channel [133].

To fulfill the demands for better design of such microfluidic devices, it is of great importance to understand the transport mechanism of microfluidic two-phase flow. Therefore, the sensing of microfluidic two-phase flow, especially for on-chip sensing, becomes interested for the researchers of diverse areas.

In this chapter, a capacitive microfluidic two-phase sensor is presented based on an overview of the microfluidic sensing. Details of the microfluidic two-phase flow sensor design, modeling, simulation, test and results are described in the following sections.

### 3.1 Overview of microfluidic two-phase flow sensing

Similar to the studies on two-phase flow in conventional channel [134], researchers have spent efforts to reveal the two-phase flow behavior inside microchannels by flow regime maps, including gas-liquid flow and immiscible liquid-liquid flow.

#### 1. Flow regime of gas-liquid two-phase flow

Zhang et al. (2011) [135] carried out experimental investigations of gas-liquid two-phase flow in circular channels by use of high-speed photography system; flow patterns such as bubbly flow, slug and unstable slug flow, churn flow, slug-annular and annular flow are observed and identified on the flow regime maps. Wang et al. (2012) [107] conducted experimental investigations of gas-liquid two-phase flow regimes in microchannels. Four distinctive flow patterns of slug flow, slug-annular flow, annular flow and parallel stratified flow were captured by a digital video recording (DVR) system and the transitions among different flow

regimes were studied. Sur and Liu (2012) [136] conducted experimental study of the effects of channel size and superficial phasic velocity on the two-phase flow pattern of air/water mixture in circular microchannels with inner diameters of 100, 180 and 324  $\mu\text{m}$ . Four basic flow patterns, namely, bubbly flow, slug flow, ring flow and annular flow, were observed; the two-phase flow regime maps were constructed and the transition boundaries between different flow regimes identified.

## 2. Flow regime of liquid-liquid two-phase flow

Dreyfus et al. (2003) [137] observed oil/water two-phase flow patterns in microchannels: at low flow rates of both water and oil, pearl necklace flow pattern was observed; while water flow rate was increased, pears shape was found. At high flow rate of oil and low flow rate of water, isolated water droplet flow occurred; while at both high flow rates, the two-phase flow pattern was stratified. Salim et al. (2008) [138] identified droplet flow, slug flow and annular flow in oil-water two-phase flow with water as the dispersed phase; while with oil as dispersed phase, droplet flow, semi-stratified flow and stratified flow were recognized. Sarkar et al. (2012) [139] studied water/succinic acid-n-butanol two-phase flow patterns in a serpentine glass microchannel using a camera with very high shutter speed. Flow regime maps were presented with seven flow patterns observed. Tsaoulidis et al. (2013) [140] studied two-phase flow of a hydrophobic ionic liquid and water in capillaries made of three different materials (two types of Teflon, FEP and Tefzel, and glass) with sizes between 200  $\mu\text{m}$  and 270  $\mu\text{m}$ .

In order to construct a flow regime map of microfluidic two-phase flow system, visualization techniques including microscope, CCD camera and even high-speed camera have often been employed [141-143]. On the one hand, the traditional visualization system that involves macro-scale optical infrastructures for optical sensing brings in more cost and less flexibility [144]. On the other hand, the on-chip approach of optical sensing for microfluidics, known as micro-optical electromechanical systems (MOEMS), demands more integration of both fluidic elements and optical elements such as movable mirror arrays, refractive microlenses, and optical filters, *etc.* [145], which consequently result in new challenges of system integration and fabrication process compatibility. Moreover, the classification of flow patterns based on captured optical images is inevitably affected by the subjective judgment. Therefore, optical sensing technique might be not the perfect solution for microfluidics devices in the very near future.

To overcome the disadvantages of optical sensing, capacitive detection is an alternative solution for two-phase flow pattern detection, due to its features of simple and non-invasive, allowing real time indication of flow patterns.

The capacitive sensing technique has been used for two-phase flow in channels of conventional size. With the aim to estimate the area fraction occupied by each fluid in pipes, Demori et al. (2010) [146] reported a capacitive sensing system for oil-water flow in a circular channel, which has an inner diameter of 19.88 mm and wall thickness of 2.0 mm. In



their work, a modified parallel-plate capacitance was mounted on the external surface of a nonconductive section of the pipe.

When the channel dimension lowers down to micro scale, there appears more room of capacitive sensing compared with the conventional channel. Chen et al. (2004) [63] proposed a miniaturized coplanar capacitive sensor, which was capable of detecting droplet position, size, composition or percentage water uptake for hygroscopic liquids. Elbuken et al. (2011) [57] investigated the presence, size and speed of microdroplets in microfluidic devices by use of capacitive sensor. Nie et al. (2012) [147] reported capacitive detection and control of microfluidic droplets in microchannels by installing a pair of parallel electrodes across the microchannel. Gijsenbergh and Puers (2013) [148] presented simulation and experimental study of capacitive void fraction sensors for microfluidic two-phase flow, which was proved to behave quite linearly with an output signal sensitivity of  $-12.5$  mV per percent void fraction for air/water two-phase flow.

According to the available literatures, it appears that most of relevant investigations focuses on the microfluidic droplet, addressing the presence, size and speed of droplets; however, quite few researches have concerned the other flow patterns apart from droplets. Owing to the diversity of microfluidic two-phase flow patterns, it demands a universal tool which is capable of identifying a specific flow pattern from the others for the microfluidic two-phase flow.

To explore microfluidic two-phase flow sensing, we proposed an integratable flow pattern sensor by employing interdigital electrodes (IDEs) and thin dielectric film. This capacitive flow pattern sensor can be integrated into complicated microsystems as *in-situ* monitoring of the microfluidic two-phase flows, for either liquid-liquid flow or gas-liquid flow.

### 3.2 Working principle

The microfluidic two-phase flow pattern sensor operates based on capacitance variation that is caused by two-phase flows, which include continuous and dispersed phases having different dielectric properties. A certain two-phase flow pattern shall have specific phase fractions, consequently corresponding to a specific capacitance value of the sensor. Therefore, the information of the detected capacitance variation can be used to identify the corresponding flow pattern.

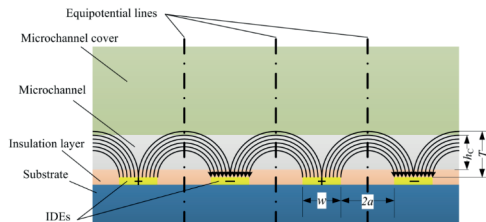


Figure 3.1 Schematic of the two-phase flow patterns sensor.

### 3.2 Working principle

The flow pattern sensor comprises of glass substrate, electrodes, insulation layer, and microchannel, as is schematically shown in Figure 3.1. The electrodes were patterned in the format of IDEs due to its coplanar feature [56]. The insulation layer was used to prevent direct contact between the fluids and electrodes, so that the electrodes would not be contaminated or shortened by the fluids.

Define the initial capacitance  $C_{\text{high}}$  and  $C_{\text{low}}$ , representing the capacitance value of the sensor when the microchannel is occupied by single phase fluid with relatively high/low permittivity, respectively. When the two-phase flow involving two fluids with different permittivity, the maximum capacitance variation should be  $(\Delta C)_{\text{max}} = C_{\text{high}} - C_{\text{low}}$ . If we define the total capacitance with certain stable two-phase flow pattern in the microchannel,  $C_{\text{TP}}$ , it is apparent that  $C_{\text{TP}}$  should fall into the range  $C_{\text{low}} \leq C_{\text{TP}} \leq C_{\text{high}}$ .

As the two-phase flow pattern in the microchannel varies (i.e., the phase fraction varies), the total capacitance will change accordingly. Here we take oil-water two-phase flow pattern as an example. Consider typical oil-in-water flow patterns in the microchannel with water as the continuous phase, namely, droplet flow, short slug flow, and long slug flow, and the corresponding capacitance variation can be roughly predicted as illustrated in Figure 3.2.

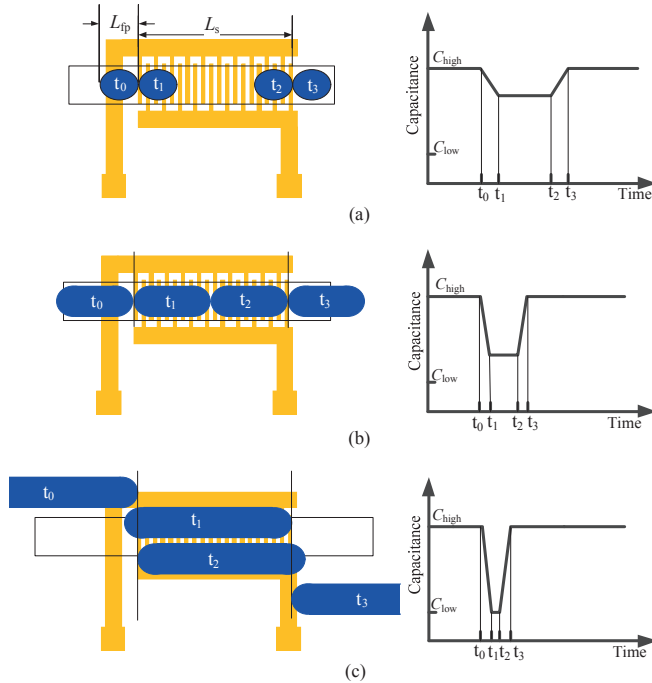


Figure 3.2 Typical oil-in-water two-phase flow patterns and the corresponding capacitance variation at different time points (flow direction: from left to right): (a) droplet flow; (b) short slug flow; (c) long slug flow.

As denoted in Figure 3.2,  $t_0$  is the moment at which the head of flow pattern structure is approaching the sensing area.

- **For droplet/short slug** (Figure 3.2(a), (b) ),  $t_1$  is the moment that whole flow structure fully enters the sensing area;  $t_2$  is the moment that the head of feature structure approaches the end of sensing area;  $t_3$  is the moment that the end of flow pattern structure leave the sensing area.
- **For long slug** (Figure 3.2(c)),  $t_1$  is the moment that the head of flow structure approaches the end of sensing area;  $t_2$  is the moment that end of the flow pattern structure is passing the entrance of the sensing area;  $t_3$  is the moment that the end of the flow pattern structure is leaving the sensing area.

The time intervals are defined as,

$$\Delta t_1 = t_1 - t_0 \quad (3.1a)$$

$$\Delta t_2 = t_2 - t_1 \quad (3.1b)$$

$$\Delta t_3 = t_3 - t_2 \quad (3.1c)$$

Moreover, we define the length of sensing area,  $L_s$ , the length of flow pattern structure,  $L_{fp}$ , and mean velocity of the flow pattern structure,  $\bar{v}$ .

Hence, for droplet/short slug, it has,

$$\bar{v} = \frac{L_{fp}}{\Delta t_1} = \frac{L_s}{\Delta t_2 + \Delta t_3} \quad (L_{fp} \leq L_s) \quad (3.2a)$$

For long slug, it has,

$$\bar{v} = \frac{L_s}{\Delta t_1} = \frac{L_{fp}}{\Delta t_1 + \Delta t_2} \quad (L_{fp} > L_s) \quad (3.2b)$$

The sensing length is known when the sensor is designed. And the time intervals can be determined according to the plot of capacitance variation versus time. Therefore, the mean velocity and the length of flow pattern structure can be easily determined with regard of (3.2). If we further introduce two dimensionless variables, the reduced length,  $L'$ , and the time ratio,  $\tau$ , as,

$$L' = L_{fp}/L_s \quad (3.3a)$$

and

$$\tau = \Delta t_2/\Delta t_1 \quad (3.3b)$$

(3.2) can further yield,

$$L' = \begin{cases} \frac{1}{1+\tau}, & \text{for } L' \leq 1 \\ 1+\tau, & \text{for } L' > 1 \end{cases} \quad (3.4)$$

The relationship of the reduced length and time ratio is plotted in Figure 3.3, in which the blue line indicates the long slug while the red curve indicates droplet and short slug.

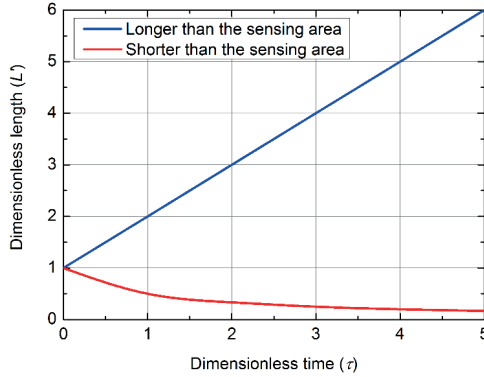


Figure 3.3 Reduced length versus time ratio.

According to Figure 3.3, when we have the profile of capacitance variation versus time, it is convenient to identify droplet from the long slug.

Similarly, this sensor can also work for gas-liquid two-phase flow, as long as the two phases have different relative permittivity.

### 3.3 Simulation of capacitance sensor for air-water two-phase flow

#### 3.3.1 Simulation model and settings

To verify the working principle for gas-liquid two-phase flow, a simulation work of the capacitance variation was performed by utilizing the commercial software COMSOL Multiphysics Ver.4.3. The simulation domain is shown in Figure 3.4a, which comprises of glass substrate (400 $\mu\text{m}$  thick,  $\epsilon_r=4.7$ ), gold IDE, insulation layer (PTFE,  $\epsilon_r=2.0$ ), and PDMS cap (400 $\mu\text{m}$  thick,  $\epsilon_r=2.8$ ). In the microchannel (400 $\mu\text{m}$  wide, and 200 $\mu\text{m}$  high) sandwiched by the PDMS cap and the glass substrate, a liquid slug is restrained and the rest space of channel is filled by gas. The thickness of the insulation layer is changed to yield different initial capacitance, from 1.0  $\mu\text{m}$  to 3.0  $\mu\text{m}$ . As one of the key parameter of slug flow, the length of slug is varied to check how it will affect the two-phase flow capacitance.

Particularly, the gold IDE was treated as 2D in the simulation, whose thickness is neglected. This simplification is valid since the thickness of IDE (around 0.1  $\mu\text{m}$ ) is tiny compared with the width (several microns to several tens micron) and length (several hundred microns). And the simplified 2D IDE make the meshing process much easier but with better quality, compared with 3D model.

The geometrical parameters of the IDE used for the simulation are listed in Table 3.1.

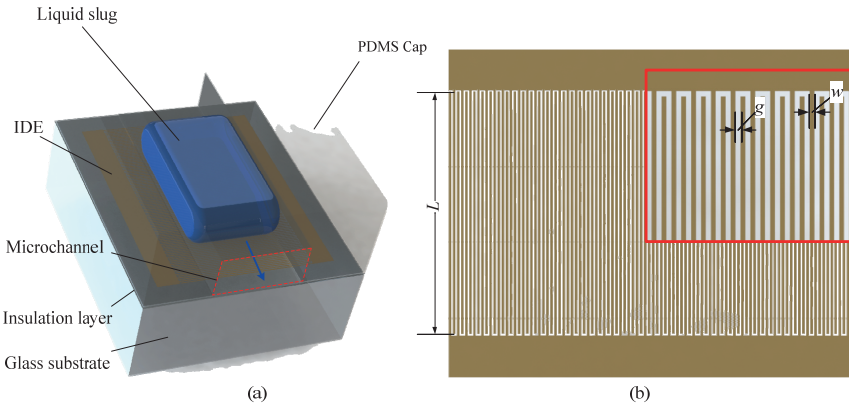


Figure 3.4 Schematic drawing of the simulation model: (a) simulation domain; (b) dimensions of the IDE.

Table 3.1 Geometrical parameters of IDEs

Case	Finger/Gap width <sup>a</sup>	Overlapping length	Finger pair number
	$\mu\text{m}$	$\mu\text{m}$	
1	5	600	50
2	10	600	25
3	20	600	13

a. The gap width is equal to the finger width,  $g=w$ .

Zero potential was set to the boundary of the simulation domain, and charge conservation was applied to the simulation model. In the simulation, the two terminals of the IDE are set at 0V and 10V, respectively, thus the capacitance between the two terminals can be checked.

### 3.3.2 Simulation results

Through FEM simulation, we can summarize the factors that the initial capacitance and capacitance depend on. More details on the simulation work can see **Paper 4** in the attachment.

#### 1. Initial capacitance

##### 1) Geometrical parameters of IDE

Table 3.2 lists the initial capacitance from the 3 cases with the microchannel filled with either air ( $C_G$ ) or water ( $C_L$ ), where the insulation layer was 2  $\mu\text{m}$  thick. It shows the initial capacitance is quite different for the microchannel filled with air or water as expected. Besides,

the maximum capacitance variation are very considerable so that they can be measured by testing.

Table 3.2 Initial capacitance with different geometrical parameters of IDEs

Case	$C_G$ (pF)	$C_L$ (pF)	$\Delta C = C_L - C_G$ (pF)	$\Delta C / C_G$ %
1	1.8930	2.5705	0.6775	35.8
2	0.8994	1.6819	0.7825	87.0
3	0.4911	0.6721	0.1810	36.8

#### 2) Insulation layer thickness

The influence on the capacitance from the thickness of insulation layer is plotted in Figure 3.5, where the geometrical parameters of Case 1 were used. It can be found that the initial capacitance for the microchannel filled with either water or air, goes up while the insulation layer is getting thicker. Therefore, if a proper thickness of insulation layer is chosen, it will help to achieve a suitable initial capacitance.

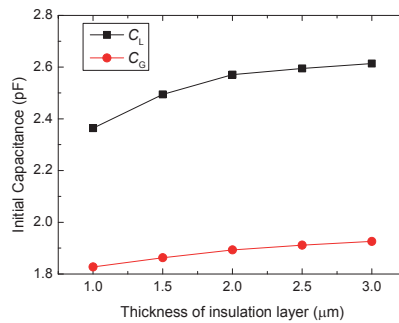


Figure 3.5 Initial capacitance varies with the thickness of the insulation layer.

#### 3) Capacitance responding to typical flow patterns

Figure 3.6 plots the capacitance change as the length of the liquid droplet varies, which indicates the different flow pattern. Particularly, for the liquid slug with the length reduced below 200 μm, the slug is treated as a ball-shaped droplet since no confinement was exerted by the channel wall. As the slug length increases from 150 μm to 900 μm, the capacitance increases from 1.9 pF to 2.2 pF. This proves that the capacitance change corresponding to the two-phase flow pattern is considerable, thus the working principle of the sensor can be verified.

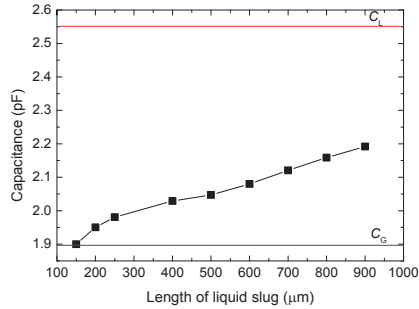


Figure 3.6 Capacitance responses with respect to various liquid slug length.

## 3.4 Prototype of two-phase flow pattern sensor design and fabrication

### 3.4.1 Design considerations

**The initial capacitance:** According to the simulation results, the initial capacitance of the sensor depends on the geometrical dimensions, such as the finger width, gap width, and the permittivity of the mediate layer. Besides, the initial capacitance is dramatically influenced by the thickness of the insulation layer. Thus it is essential to determine all the related parameters to yield a proper initial capacitance.

**The capacitance corresponding to a certain two-phase flow pattern:** To identify the basic two-phase flow patterns inside the microfluidic systems, e.g., bubbly flow, short slug flow, and long slug flow, the capacitance variation caused by each flow pattern should be comparable with the initial capacitance, so that it is detectable.

**The penetration length:** Consider the channel height  $h_c$  shown in Figure 3.7. While penetration length  $T < h_c$ , the permittivity of the fluid layer will affect the capacitance more than the permittivity of the PDMS cap; while  $T > h_c$  the effect from the permittivity of the PDMS will have to be included. Therefore, the penetration length should be well designed to identify each flow pattern. To make sure all the features of flow pattern inside the microchannel sensible, the height of microchannel was determined by  $h_c < T$ .

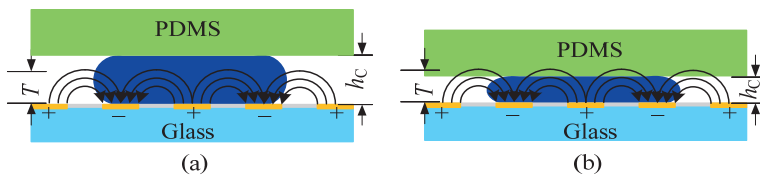


Figure 3.7 Relationship between the penetration length and the thickness of the liquid phase: (a)  $T < h_c$ ; (b)  $h_c < T$ .

### 3.4.2 Design and microfabrication

Figure 3.8(a) illustrates the structure of the flow pattern sensor. To evaluate the influence of dimensions of IDE finger in identification of two-phase flow patterns, three sets of IDEs with different geometrical parameters (six units in total) are listed in Table 3.3. In addition, each IDE unit contains four contact pads, allowing changing the number of fingers (i.e., the sensing area) involved in measurements. One of the contact pads is fixed and the others are optional. A thickness of  $2.0\ \mu\text{m}$  for the insulation layer was determined as a compromise between an appropriate total capacitance and reliable insulation.

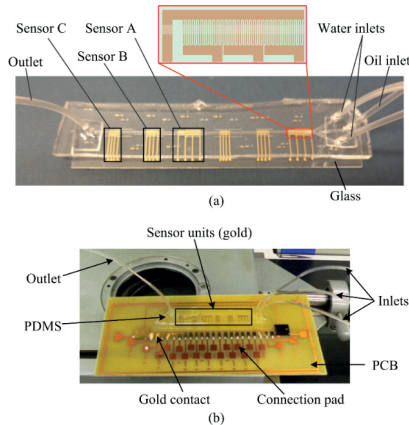


Figure 3.8 Prototype of flow pattern sensors: (a) Optic photo; (b) Prototype fixed on the PCB board with the electric connections via wire bonding.

Table 3.3 Geometrical Parameters of Capacitive Sensors

Geometrical Parameters	Sensor A	Sensor B	Sensor C
Finger width, $w$ ( $\mu\text{m}$ )	50	5	4
Finger gap width, $2a$ ( $\mu\text{m}$ )	50	5	4
Length of finger overlap, $l$ ( $\mu\text{m}$ )	850	850	850
Number of finger pairs (per sensing unit)	10	50	50

The prototypes were fabricated on a glass wafer with patterned gold IDEs ( $0.1\ \mu\text{m}$  thick). A  $2\ \mu\text{m}$ -thick insulation layer of SU-8 coated the glass wafer on top of IDEs. Then a PDMS cover with a microchannel was molded and bonded on the insulation layer. Thus a microchannel for two-phase flow forms, which is  $150\ \mu\text{m}$  high and  $800\ \mu\text{m}$  wide. Three inlets allow input of fluids inside the microchannel. For convenience to electric connection, wire bonding is used to connect the contact pads and a printed circuit board (PCB), allowing further change of signal processing from the sensor. The wires were bonded to gold contacts, glued onto the board by silver epoxy. More details of the fabrication process can be found in **Paper 4**.



## 3.5 Experiment of oil-liquid two-phase flow

### 3.5.1 Experimental setup and test procedure

The two-phase flow experiments were performed with deionized water (continuous phase) and olive oil (dispersed phase), with the relative permittivity,  $\epsilon_w=80$ , and  $\epsilon_o=2.4$ , respectively. And the test system is shown in Figure 3.9.

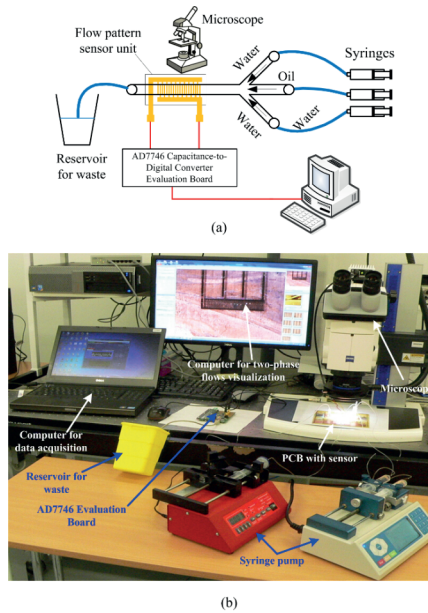


Figure 3.9 Experimental system setup: (a) Schematic arrangement; (b) Photo during the test.

Water and olive oil were driven by individual syringe pumps, thus the flow-rates of liquids can be precisely set in the syringe pumps. Microbore tubes (Tygon®) with the outside diameter of 1.5mm and inner diameter of 1mm were used to lead the liquid from the syringe to the inlets of prototype. To make sure that water should be the continuous phase, the water was pumped by two syringes in parallel, which was then led into the two lateral inlets; and the central inlet was used for olive oil.

The flow patterns were observed and recorded by a visualization system, which comprises of a Zeiss® SteREO Discovery V12 microscope and Digital Microscopy Camera AxioCam ICc 5 connected to a computer.

Before test, the microchannel was saturated with water in advance. During test, the flow rates of water and olive oil were kept constant for a period (around 5 minutes) to develop a stable flow pattern. When the flow pattern was completely developed, responses from one

sensing unit, and two sensing units were checked, respectively. Both signal acquisition and image capture were performed at the same time, but in different computers.

### 3.5.2 Capacitance-to-Digital Converter

In order to read the capacitance variation caused by different flow patterns, AD7746 capacitance-to-digital converter (CDC) (Analog Devices, Inc. 2005) was used to extract the signal from the electrodes, as shown in Figure 3.10 [149]. The measured capacitance was connected directly to the device inputs. An AD7746 evaluation board is shown in Figure 3.10b. AD7746 provides two individual measurement channels, featuring inherent a 24-bit resolution. The full-scale linear ( $\pm 0.01\%$ ) capacitance measurement range of AD7746 is  $\pm 4$  pF with a precision of 4fF, and it is possible to accept a higher capacitance up to 17 pF with programmable on-chip, digital-to-capacitance converter (CAPDAC) mode.

For this work, as the capacitance of both one sensing unit and two sensing units were no more than 4.096 pF with the water in the micro-channel, it is not necessary to involve CAPDAC mode.

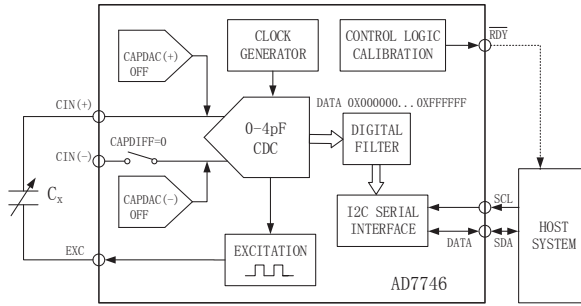


Figure 3.10 Simplified functional diagram of the AD7746 Capacitance-to-Digital Converter, Analog Digital [149]

### 3.5.3 Data acquisition

To obtain a real-time data of the measured  $C_x$ , a USB-powered microcontroller (Cypress, CY7C68013A-56LFXC) was used to establish communication between the evaluation board and the computer; and the real-time capacitance variation was displayed by the AD7746 Evaluation Software.

The sampling rate of AD7746 can be changed between 10 Hz and 90 Hz with corresponding root mean square noise levels of 4.2 aF and 40 aF. In this work, the sampling rate was selected at 32.2 Hz, so as to remove the 50/60 Hz power-line interference. For each measurement, 322 data samples were acquired (about 10s) and recorded in the continuous conversion mode. The relation between the capacitance input and data code can be expressed as,

$$C_x = \frac{CODE - 2^{23}}{2^{23}} C_{ref} \quad (3.5)$$

where  $C_{ref}$  is the internal reference capacitance,  $C_{ref} = 12.288$  pF; *CODE* is the original data acquired from the software, which is a series of hexadecimal data.

## 3.6 Experimental results of oil-water two-phase flow pattern sensing

### 3.6.1 Typical oil-water two-phase flow patterns

Different flow-rates of water and oil have been tried to obtain various flow patterns in the experiments. Some typical flow patterns were observed through the visualization system, namely, droplet flow, short slug flow, long slug flow and annular flow, as illustrated in Figure. 3.11. Here we distinguish the different flow patterns in terms of the length of the flow structure. For the droplet flow, the feature length should be less than twice of the channel width ( $1600\mu\text{m}$ ); the length of short slug should be less than twice length of single sensing unit in sensor A ( $3900\mu\text{m}$ ), equal to three active units; otherwise it is considered as long slug. The annular flow pattern is characterized by presence of an oil annulus in water sliding walls.

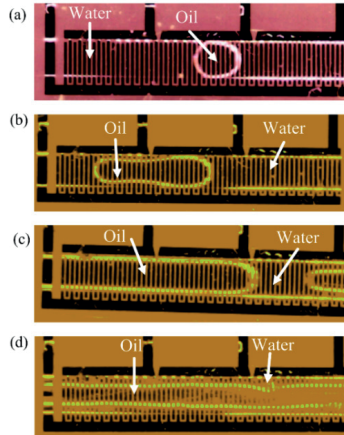


Figure 3.11 Typical flow patterns in the microchannel. (a) Droplet flow,  $Q_o=0.001\text{mL/min}$ ,  $Q_w=0.005\text{mL/min}$ ; (b) Short slug flow pattern,  $Q_o=0.003\text{mL/min}$ ,  $Q_w=0.03$  mL/min. (c) Long slug flow pattern,  $Q_o=0.004$  mL/min,  $Q_w=0.06$  mL/min; (d) Annular flow,  $Q_o=0.005$  mL/min,  $Q_w=0.1$  mL/min.

The droplet flow pattern occurs when both superficial velocities are rather small. In the droplet flow, the oil droplet takes on a nearly round/oblong shape, with the diameter close to the width of the microchannel. As the superficial velocity of oil rises, the droplet will get elongated and turn to be a short slug. A long slug flow pattern will occur while further increasing the oil velocity. While the superficial velocity is relatively larger, the annular flow

occurs, in which the oil flow becomes continuous occupying the center of the microchannel. A flow pattern map was summarized based on the observation of flow pattern images during the test, as shown in Figure 3.12.

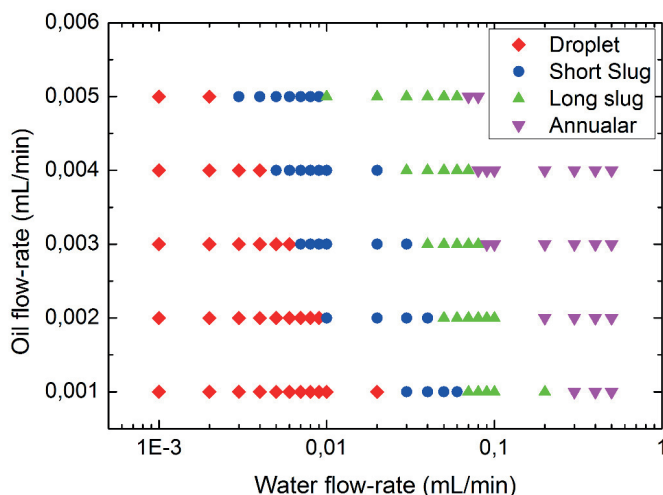


Figure 3.12 Flow pattern map, with y- oil flow-rate and x-water flow-rate.

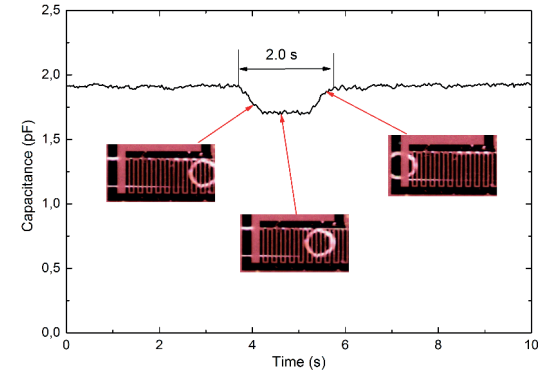
It was found that the annular flow occurs at larger velocity/ higher Reynolds number for both water and oil. For microfluidic flow in lab-on-chip devices, most of the flows fall into laminar flow range with Reynolds number lower than 1, which means no chance to be developed into an annular flow. Therefore, we focused on the intermittent flow, such as droplet flow, short slug flow, and long slug flow, neglecting the annular flow in this work.

### 3.6.2 Typical capacitance variation with respect to typical flow patterns

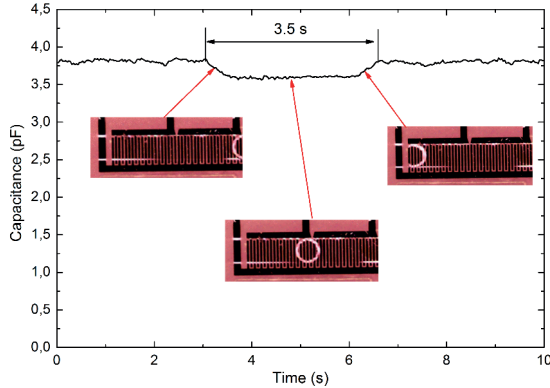
#### (1) Droplet flow

Figure 3.13 illustrates the typical capacitance variation when the droplets pass the sensing area. In Figure 3.13a, only one unit in sensor A was employed. When the curved front of the droplet entered the sensing unit, a decreasing capacitance was observed with an approximate magnitude of 0.2 pF. While the droplet traveled through the sensing area, the capacitance kept the magnitude (since there is no variation in the volume of oil in the droplet) but with small fluctuations. These fluctuations can result from noise or two-phase interface variation due to the interactions between oil and water phase. When the droplet left the sensing area, the capacitance gradually increased to the initial value. When only water was on top of the sensing area the output signal remained closer to 1.9 pF.

In Figure 3.13b, two units of sensor A were connected in series to sense the droplet flow. The maximum capacitance was around 3.8 pF. Similar information on the droplet dynamics can be deduced from Figure 3.13b. Compared with Figure 3.13a, the time period for a droplet traveling through the sensing area with two units is almost doubled, because of the doubled sensing length of the sensor. Besides, the magnitude of the capacitance variation was almost the same with each other.



(a)  $Q_o=0.001$  ml/min,  $Q_w=0.005$  ml/min (droplet length=676  $\mu\text{m}$ , deduced from the curve)



(b)  $Q_o=0.001$  ml/min,  $Q_w=0.005$  ml/min (droplet length=625  $\mu\text{m}$ , deduced from the curve)

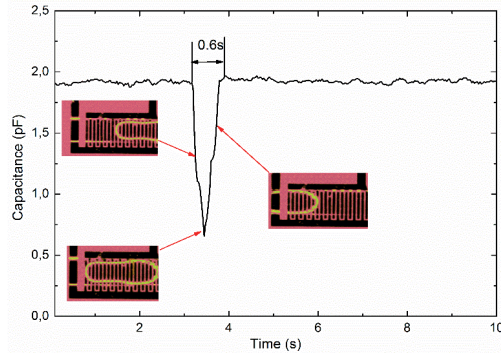
Figure 3.13 Capacitance of droplet flow with sensor A (Flow enters the sensing area from the right to the left): (a) one sensing unit; (b) two sensing units.

## (2) Short slug flow

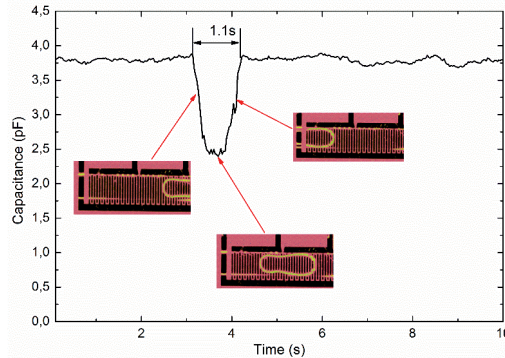
The typical capacitance variation for short slug flow is plotted in Figure 3.14. Since the slug begin to enter into the sensing area, the capacitance value decreases sharply and immediately increases again to the original value (Figure 3.14a). When the short slug almost stay inside the sensing area, there was a decrease in the capacitance value of approximately 1.2 pF. When two sensing units were used, due to the larger length of the sensing area, the maximum capacitance become around 3.8 pF, and the time that the short slug passed through the sensing

### 3.6 Experimental results of oil-water two-phase flow pattern sensing

area was increased to 1.1 s (Figure 3.14b), which was longer than that in one sensing unit (about 0.6 s). While the short slug traveled through the sensing area, the capacitance also kept the amplitude with small fluctuations, which was similar as the droplets. When the short slug leave the sensing area, the capacitance also returned to the initial value.



(a)  $Q_o=0.003$  ml/min,  $Q_w=0.03$ ml/min (short slug length 1950  $\mu\text{m}$ , deducted from the curve)



(b)  $Q_o=0.003$  ml/min,  $Q_w=0.03$ ml/min (short slug length 2049  $\mu\text{m}$ , deducted from the curve)

Figure 3.14 Capacitance variation of short slug flow with sensor A (Flow enters the sensing area from the right to the left): (a) one sensing unit; (b) two sensing units.

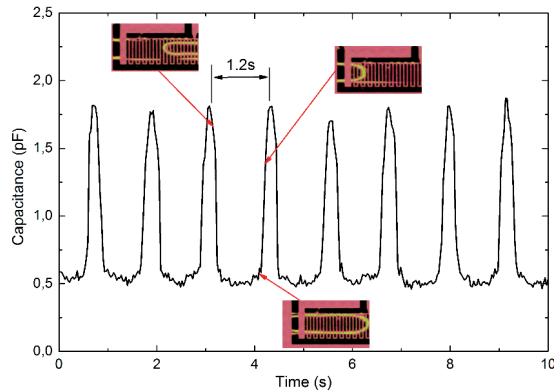
Comparing Figure 3.13 and Figure 3.14, it is found that the droplet flow and short slug flows have the different amplitude of capacitance variation. Concerning the amplitude of the capacitance variation, it has been clearly shown that the amplitude of the short slug are much larger than the droplets, because the short slugs, having a longer length than the droplets, have larger volume fraction in the sensing area, leading to a larger capacitance decrease. As for the capacitance variation profile, the short slug has a longer length, meanwhile the short slug flow is associated to higher flow rates; therefore it is difficult to compare the time period to identify the two flow patterns.

As the data obtained for droplet flow pattern and the short slug are very similar, it is not possible to directly identify the flow patterns merely based from the acquired curves without

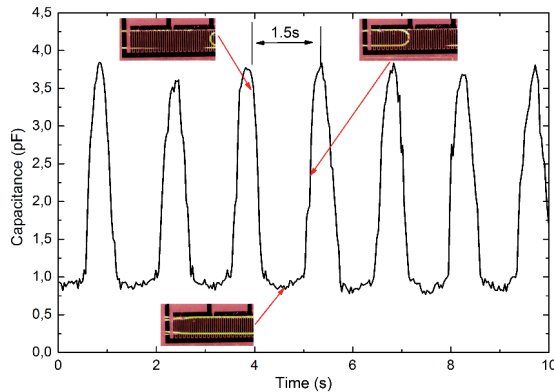
knowing the specified amplitude of capacitance variation. Some specific techniques have to be figured out to identify the flow patterns.

### (3) Long slug flow

For the long slug flow, the typical capacitance variation is depicted in Figure 3.15. When a long slug enters the sensing area, there is a quick decrease in the capacitance, followed by a more or less stable capacitance. When the long slug leaves the sensing area, the capacitance is increased again; however, the capacitance is not well recovered because immediately another long slug enters the sensor. Therefore, the peaks of capacitance indicate very short water plugs between the two long oil slugs. When one unit was used (Figure 3.15a), the time interval the signal remained in low levels was approximately 1.2 s and when two units are active that time interval is increased to 1.5s. Additionally, the amplitudes of capacitance decrease are around 1.3 pF and 2.7 pF when one unit and two units are used, respectively.



(a)  $Q_o=0.005\text{ml/min}$ ,  $Q_w=0.06\text{ml/min}$  (long slug length  $6332\ \mu\text{m}$ , deducted from the curve)



(b)  $Q_o=0.005\ \text{ml/min}$ ,  $Q_w=0.06\text{ml/min}$  (long slug length  $6481\ \mu\text{m}$ , deducted from the curve)

Figure 3.15 Capacitance of long slug flow with sensor A: (a) one sensing unit; (b) two sensing units. (Flow enters the sensing area from the right to the left).

According to Figure 3.15, a clear difference in the profile of the data is observed for long slug flow, compared to those of droplet and short slug flows. The frequency of the dispersed phase is much higher, which means more slugs were recorded during the sampling period. This is due to the higher flow rates of the two phases in the inlets associated to the long slug flow.

### 3.6.3 A characteristic number distinguishing flow patterns

Considering the similarity of flow patterns, we can understand that the capacitance variation profiles are very similar between the droplet and short slug, especially for those of droplet in one sensing unit and short slug in two sensing unit. Of course the magnitude of capacitance variation is different for droplet and short slug. The droplets (Figure 3.13) having short flow structures, are commonly associated to low flow rates, resulting in the sensing area for a longer time; the short slugs (Figure 3.14) have longer flow structures but associated to higher flow rates, which makes short slugs remain in the sensing area for a time period very similar to that of the droplets. As for the time period, for the droplet and the short slug flow patterns, there is a “compensation” between the length of the structures and the time in the sensing area; for this, in the profile of capacitance variation, the droplet and short slugs flow pattern appear to be very similar.

We may try to find another way to identify the flow patterns more directly. According to Salim et al. [138], a linear relationship to identify a constant that allows to distinguish different flow patterns can be written as,

$$D_0 = \frac{\bar{v}}{J_w + J_o}, \quad (3.5)$$

where  $J_w$  and  $J_o$  are the superficial velocities of water and oil, respectively, obtained by the flow rate in the inlets;  $\bar{v}$  is the measured velocity and  $D_0$  is a constant that depends on the flow pattern. In this work,  $\bar{v}$  can be calculated by (3.2). For example, consider the data in Figure 3.13a: the time for the droplet to travel through one sensing unit is approximately 1.5 s and the length of the sensor is 1950  $\mu\text{m}$ . Therefore,  $v_{\text{meas}}$  will be calculated at 0.0013 m/s.

With the already known flow rates of each phase, the superficial velocity of each phase can be calculated by the ratio of the volumetric flow rate by cross-sectional area of the microchannel; and afterwards the value of  $D_0$  can be calculated by (3.5). Figure 3.16 plots several values of  $D_0$  from different sets of data for each flow pattern. Additionally, a mean value of  $D_0$  of each flow pattern is also calculated by arithmetically averaging.



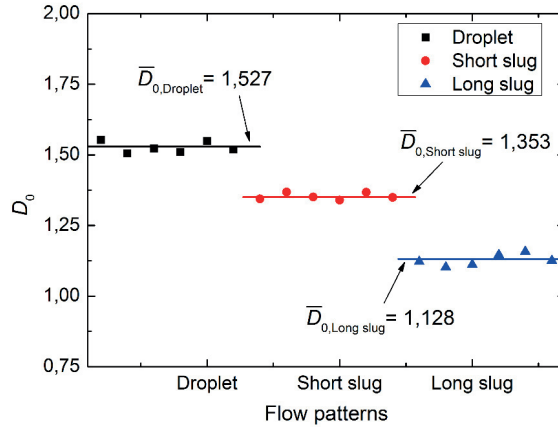


Figure 3.16 Values of the constant that is directly related to the flow patterns. The square markers represent the average value of  $D_0$  and the error bars represent the minimum and maximum values.

According to Figure 3.16, a characteristic constant of  $D_0$  for each flow pattern, with small variation of values, as shown by the dots, is obtained. This indicates that the sensor can identify important features to recognize the flow patterns, specifically the time of the dispersed phase remains in the sensing area. Additionally the sensor provides the length value, by previous knowledge of the geometrical characteristics of the sensing units in each sensor.

The values of  $D_0$  will also be related to the geometrical features of the microchannel. For this reason, the calculated values of  $D_0$  can only be used as reference values for this specific microchannel; for other microchannels, the values could vary and have to be calibrated to specify.

More results and discussion on the two-phase flow pattern sensor can be found in **Paper 5** attached.



# Chapter 4

## Conclusions and prospects

### 4.1 Conclusions

In this thesis, explorations into the microfluidic transduction and sensing by use of interdigital capacitance (including interdigital electrodes and thin insulation film) have been conducted. With microfabrication compatibility and cost-effectiveness taken into consideration, the coplanar interdigital capacitance has shown promising capability of non-intrusive transduction and sensing for microfluidics. As two applicable cases of interdigital capacitance, a fluidic electrostatic energy harvester and a microfluidic flow pattern sensor have been developed.

The fluidic electrostatic energy harvester employing droplet/IL marbles rolling through interdigital electrodes are demonstrated with simulation, modeling, and experimental verifications. A very thin electret film being achieved with charges embedded during sputtering, no extra process of charging is required. Mercury droplets as well as IL marbles were used to demonstrate the function of the prototype. As has been demonstrated, the output performance of electrostatic energy harvester employing mercury droplet is quite considerable. The output voltage with peak value above 1.5 V is in a suitable range to be dealt with by power conversion electronics and energy storage. While a cyclic tilting of the device where a half cycle corresponds to one traversal of the IDE by the droplet is considered, the measured output energy for a 1.2-mm mercury droplet in the device amounts to 3.0nJ per cycle per droplet. This can be favorably comparable to the previous work by Boland et al. [115] with 0.17 nJ per cycle per droplet.

A semi-empirical model has been developed to explain the operation of fluidic electrostatic energy harvester. Dynamic behaviors of the rolling droplet/IL marbles have been explored based on the test data. It is found that both the mercury droplet and IL marble behaves approximately like a “free-fall” solid ball. It is observed that the droplet size, inclination angle of the device, and the match between the droplet size the electrode finger width affect the output performance of the energy harvester. Such conductive droplet/marbles based electrostatic energy harvester is suitable for very low frequency vibration, such as human motion.

With the aim to distinguish typical microfluidic two-phase patterns, a microfluidic flow pattern sensor has been developed, which is also based on interdigital electrodes and thin insulation film. Differing from the microfluidic electrostatic energy harvester, the insulation film in the microfluidic flow pattern sensor was made of SU-8 by spinning coating. Simulation results show that the thickness of the insulation film and dimensions of interdigital electrodes have significant influence upon the initial capacitance of the sensor. Therefore,

with a compromise between sufficient insulation and appropriate initial capacitance, the thickness of the insulation film was well controlled through adjusting the spinning frequency.

A prototype of microfluidic flow pattern sensor that is capable of detecting presence of different flow patterns in microchannels has been demonstrated. For three typical flow patterns, droplet, short slug and long slug flows of olive oil-water two-phase flow, time-dependent capacitance variation corresponding to each flow pattern were obtained from the prototype. It was observed that the  $c$  of the long slug flow differs very well from those of the two other flow patterns, thus the long slug flow can be easily identified in terms of the output signal. Even though the output signals for the droplet flow and short slug flow were found being similar, additional methods were employed to distinguish these two flow patterns. The calculation of a constant specific for a given flow pattern through a linear relation can give clear identification for each flow patterns. Therefore, this microfluidic flow sensor can be used to identify the typical two-phase flow patterns, comprising of two immiscible fluids whose relative permittivities are remarkably different, no matter liquid-liquid flow, or gas-liquid flow, even vapor-liquid flow. Besides, this microfluidic flow pattern sensor can be easily integrated into complicated microfluidic devices for *in situ* sensing.

### 4.2 Prospects

With the more and more emergences of novel microfluidic devices in the coming years, challenges of microfluidic transduction and sensing shall increase in various specific application scenes. The feature of non-intrusive will be still required for microfluidic transduction and sensing technique. Coplanar interdigital capacitive sensing for microfluidics shall be one of competitive solutions due to its perfect microfabrication compatibility.

The fluidic electrostatic energy harvester presented in this thesis can be further developed into a practical prototype with droplets/marbles sealed inside. While employing mercury droplet, the output power of the energy harvester can be increased by adding more of droplets. Therefore, further investigations, such as, design of rolling track configuration for multiple droplets, sealing of the droplets system, performance optimization of the prototype are to be conducted. While employing IL marbles, challenges lie in how to make the PTFE powders uniformly coating the surface of marble therefore reducing the “surface roughness” and increasing the output voltage, and how to design the prototype to prevent the IL marbles from crushing when colliding the sidewall, etc.

The capacitive microfluidic flow pattern sensor has been demonstrated for typical flow patterns in microchannels. However, the flow patterns presented in the thesis are the simplest cases: only one flow structure was involved in the sensing area, that is, only one droplet or short slug appears in the sensing area. When two or more flow structures pass the sensing area during the test period, the results would be more complicated, which require further investigations. Besides, the capacitive microfluidic flow pattern sensor can be also optimized to improve the sensitivity so that it might be used for two immiscible fluids with smaller

difference of relative permittivity. This can be realized by optimizing the dimensions of electrode fingers and the thickness of insulation layer.

Moreover, the capacitive microfluidic flow pattern sensor might be developed into more complicated microfluidic sensor, e.g., content sensor recently reported by Isgor et al. (2015) [150].

To sum up, the capacitive sensing and transduction for microfluidics can be well developed in the near future together with the rapid development of microfluidic devices. More advanced applications and more specified functions of microfluidic capacitive sensing will emerge in the near future.



# Chapter 5

## List of publications

The publications listed below are based on the work that has been conducted, including 3 journal papers, 1 conference paper, and 1 manuscript submitted.

### Paper 1

Zhaochu Yang, Einar Halvorsen, Tao Dong. Power generation from conductive droplet sliding on electret film. *Appl. Phys. Lett.* 100, 213905 (2012)

### Paper 2

Zhaochu Yang, Einar Halvorsen, Tao Dong. Capacitance variation in electrostatic energy harvester with conductive droplet moving on electret film. *PowerMEMS 2013, Journal of Physics: Conference Series* 476 (2013) 012094

### Paper 3

Zhaochu Yang, Einar Halvorsen, Tao Dong. Electrostatic Energy Harvester Employing Conductive Droplet and Thin-Film Electret. *Journal of Microelectromechanical Systems*, vol. 23, no. 2, 2014, 315-323.

### Paper 4

Zhaochu Yang, Tao Dong and Einar Halvorsen. Identification of microfluidic two-phase flow patterns in lab-on-chip devices. *Bio-Medical Materials and Engineering* 24 (2014) 77–83.

### Paper 5

Zhaochu Yang, Tao Dong, Atle Jensen, Einar Halvorsen. Integratable Capacitive Sensor for Identification of Microfluidic Two-phase Flow Patterns in Lab-on-chip Devices. *Submitted to Journal of Microelectromechanical Systems*, JMEMS-2014-0360





# Paper I

**Title:** “Power generation from conductive droplet sliding on electret film”  
**Author:** Zhaochu Yang, Einar Halvorsen, and Tao Dong  
**Journal:** Applied Physics Letters  
**Year:** 2012  
**Volume:** 100  
**Number:** 21  
**Pages:** 213905



## Power generation from conductive droplet sliding on electret film

Zhaochu Yang, Einar Halvorsen,<sup>a)</sup> and Tao Dong

Department of Micro and Nano Systems Technology (IMST), Vestfold University College, P.O. Box 2243, N-3103 Tønsberg, Norway

(Received 2 April 2012; accepted 7 May 2012; published online 23 May 2012)

Generating electrical power from low frequency vibration to power portable devices is a challenge that potentially can be met by nonresonant electrostatic energy harvesters. We propose a generator employing a conductive droplet sliding on a microfabricated electret film which is sputtered onto an interdigital electrode and charged already during deposition. Droplet motion causes a capacitance variation that is used to generate electric power. A prototype of the fluidic energy harvester demonstrated a peak output power at  $0.18 \mu\text{W}$  with a single droplet having a diameter of  $1.2 \text{ mm}$  and sliding on a  $2\text{-}\mu\text{m}$  thick electret film. © 2012 American Institute of Physics. [<http://dx.doi.org/10.1063/1.4720517>]

Energy harvesting from the environment has attracted considerable academic and industrial interest during the last decade. It is a promising power source for wireless sensors, distributed sensors, and biomedical sensors.<sup>1,2</sup> Several principles for energy conversion, such as electrostatic, piezoelectric, electromagnetic, photovoltaic, and thermoelectric transduction have been demonstrated. One notable mechanism that is particularly suited for microfabricated vibration harvesters is electrostatic transduction. It is based on motion-induced capacitance-variation under a bias provided by an external voltage or by an internal fixed charge polarization; the latter is indispensable for a self-sufficient device. The internal polarization can be obtained by extra process steps to deposit and subsequently charge a dielectric by, e.g., corona discharge, contact charging, or electron-beam irradiation to obtain an electret.<sup>3,4</sup>

Traditional electrostatic energy harvesters have spring-mass configurations whose proof-mass motion relative to a package frame drives an in-plane overlap varying, in-plane gap closing, or out-of-plane gap closing transducer.<sup>5,6</sup> They were initially designed to be operated resonantly at a specific frequency but have been further developed to adapt to broadband random vibrations by exploiting non-linear elastic behavior of the springs that suspend the mass.<sup>7,8</sup> In environments with low frequencies and large displacement amplitudes, however, the resonant energy harvesters have few, if any, advantages. Thus the conventional spring suspension has to be either made very compliant or abandoned altogether. This is the main motivation for making devices with rolling<sup>9,10</sup> or sliding<sup>11,12</sup> proof masses.

The fluids offer another solution. In addition to fluid-specific approaches such as scavenging energy from an evaporating flow,<sup>13</sup> it is also possible to utilize a fluid droplet as a proof mass. This is attractive with respect to avoiding wear and can potentially display very low friction if a sufficient contact angle is achieved. Boland *et al.*<sup>14</sup> reported a liquid-rotor electret power generator employing mercury droplets and air-filled gaps in an electret capacitor. The electret was made from a  $25 \mu\text{m}$ -thick Teflon<sup>TM</sup> fluorinated ethylene propylene (FEP) glued to an electrode. Krupenkin and Taylor<sup>15</sup>

further developed such ideas in investigating various designs of droplet arrays with an external bias. Löhndorf *et al.*<sup>16</sup> invented an electrostatic energy harvester using electrically conductive liquids, such as ionic liquids, which deform or flow within a chamber so as to change a capacitance. Several properties of ionic liquids,<sup>17</sup> e.g., their conductivity, non-volatility, and low toxicity (compared to mercury), make them attractive fluids for energy harvesting.

In this letter, an electrostatic energy harvester employing conductive droplets sliding on a thin polytetrafluoroethylene (PTFE) electret is proposed. With interdigital electrodes (IDEs) patterned beneath, a PTFE film is deposited as well as charged during a sputtering process. By this, we obtain a large capacitance and avoid later charging of the electret. The output power is achieved by letting a mercury droplet slide across the PTFE film. Furthermore, the use of ionic liquid marbles<sup>18</sup> with hydrophobic properties was also investigated. This fluidic electrostatic energy harvester is especially suitable for harvesting energy from low frequency sources such as human body motion.

The working principle of the fluidic energy harvester is based on a variable capacitance induced by a conductive droplet sliding on a charged film, i.e., an electret film, as schematically shown in Fig. 1. Beneath the electret film, there are thin electrodes patterned on a glass wafer. Given that a droplet-electrode overlap area  $A_i$  ( $i=1$  or  $2$ ) has linear dimensions much larger than the film thickness  $d$ , the droplet-electrode capacitance at time  $t$  is simply  $C_{\text{var},i} = \epsilon A_i(t)/d$ , where  $\epsilon$  is the permittivity of the insulating film. Hence, the capacitance can be devised as large as possible by making the film thin enough. This situation corresponds to the leftmost electrode in Fig. 1(a) and both electrodes in Fig. 1(b). When the droplet does not overlap with an electrode, like for the rightmost electrode in Fig. 1(a), the droplet-electrode capacitance is small and entirely given by fringing field effects. The resultant variable electrode-electrode capacitance is  $C_{\text{var}} = C_{\text{var},1} C_{\text{var},2} / (C_{\text{var},1} + C_{\text{var},2})$  which has its maximum when  $C_{\text{var},1} = C_{\text{var},2}$  and decreases to a small value when either of the capacitances go to a small value. A simplified 2-D model in COMSOL V4.2 confirms this principle. The result is shown in Fig. 2. When the droplet is located at  $x=0$ , midway between the two adjacent electrodes, the capacitance reaches

<sup>a)</sup>Electronic mail: Einar.Halvorsen@hive.no.

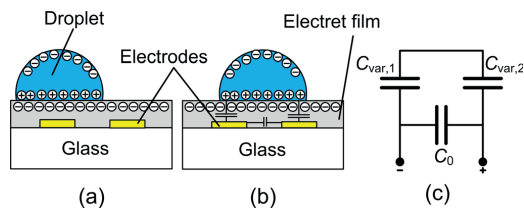


FIG. 1. Working principle of the fluidic energy harvester based on conductive droplet (not to scale): (a) and (b) indicates different droplet position vs. the IDEs and (c) equivalent circuit.

its peak value and falls to one tenth of this value when the droplet is centered on one of the electrode fingers. In practice, there is always a significant direct capacitance  $C_0$  between the electrodes, thus the total capacitance will be  $C_{\text{tot}} = C_0 + C_{\text{var}}$  as indicated in Figs. 1(b) and 1(c).

Due to the embedded electric charges in the dielectric film, the device is electrically polarized. Moreover, there will be charges on the surface of the conductive droplet that can redistribute as it rolls or slides on the electret film, e.g., from position (a) to position (b) in Fig. 1. The droplet as a whole is still charge neutral. Due to fringing fields, the motion will not only cause a capacitance variation but also generate a position dependent open circuit voltage. We verified with the 2-D model that this is the case even if there is a homogenous charge distribution in the film. Hence the device will be self-biased with a charge present in the film.

Based on the working principle described in Fig. 1, a prototype of the fluidic energy harvester was microfabricated. A 100 nm thick IDE pattern on a 4-in. Pyrex 7740 glass wafer was made by gold sputtering and wet etching. The fingers were 500  $\mu\text{m}$  wide and had 500  $\mu\text{m}$  gaps between adjacent fingers. The IDE was then coated by a 2- $\mu\text{m}$  thick PTFE film by radio frequency (RF) magnetron sputtering. The thickness of the film is a key parameter affecting the resulting capacitance. Therefore, the PTFE film thickness was controlled by repeated sputtering of thin layers in order to compromise between a reliable insulation and a considerable maximum capacitance. As the gas (Ar) atoms are ionized by RF power to strike the target, the sputtering process starts, during which the electrons were simultaneously accu-

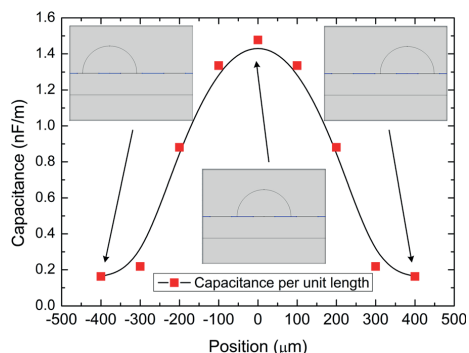


FIG. 2. Capacitance versus droplet position.

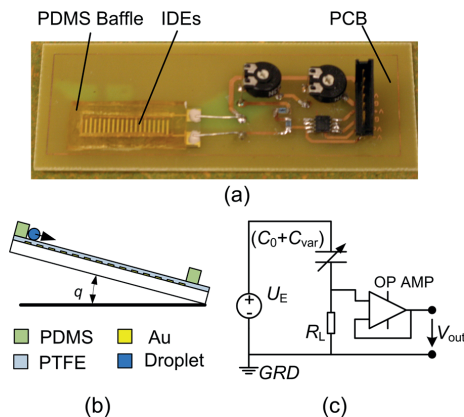


FIG. 3. Prototype and test setup: (a) optical image for prototype of fluidic energy harvester on PCB; (b) cross-section view of the prototype; and (c) schematic drawing of the test system.

mulated in the thin film. The average surface potential on the RF sputtered PTFE was measured to  $-16\text{ V}$  (after 14 months) by an electrostatic voltmeter (Isoprobe, Model 279). Hence, a charged electret film is obtained during the fabrication without any extra charging procedure. In order to prevent the droplet from sliding out of the electrode area, a solid polydimethylsiloxane (PDMS) baffle surrounding the IDEs area was attached.

For convenience of testing, the circuit was arranged on a printed circuit board (PCB), onto which the energy harvester prototype was glued as shown in Fig. 3(a). During testing, a conductive droplet was placed on the insulating film close to the left end of the IDEs. Then the PCB was tilted to a certain angle  $\theta$  (Fig. 3(b)), so that the droplet started to slide downward with a constant acceleration  $a = g \sin \theta$ . Figure 3(c) shows the setup of the test circuit. A variable load resistor set to  $R_L = 16\text{ M}\Omega$  was connected to the device. The output voltage was recorded by LabView v9.0.1 with NI-USB-6211 DAQ connected to a laptop computer. The instantaneous output power was obtained from  $P_{\text{out}} = V_{\text{out}}^2/R_L$ .

Two types of conductive droplets were employed in the experiment: mercury and an ionic liquid. The mercury was used as is. The ionic liquid was 1-ethyl-3-methylimidazolium tetrafluoroborate (EMIM BF<sub>4</sub>) and had wetting problems preventing its direct utilization. Therefore, we formed ionic liquid marbles by covering 1  $\mu\text{l}$ -droplets with PTFE powder of 1  $\mu\text{m}$  particle size.<sup>18</sup>

Fig. 4 illustrates typical dynamic output voltage across the load resistor and the corresponding output power while a mercury droplet slides across the IDEs. When the droplet starts to slide (at  $\theta \sim 15^\circ$ ), the output voltage begins to fluctuate dramatically with positive and negative peaks alternating as the droplet travels across each pair of fingers of the IDEs. As the droplet keeps accelerating from the top to the bottom, it is clear that the time difference between two sequential peaks decreases. We found that the droplet acceleration corresponds approximately to free fall behavior, i.e.,  $x \sim at^2/2$ . The maximum output voltage (and power) occurs when the droplet reaches its maximum velocity at the other

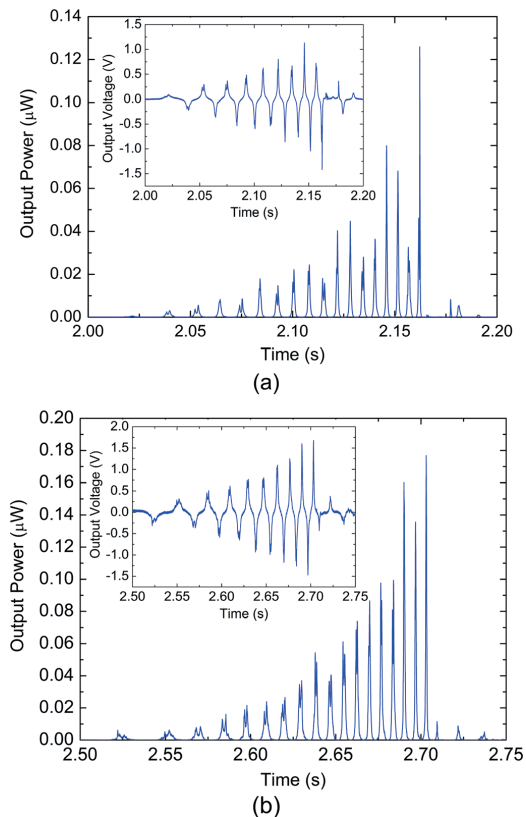


FIG. 4. Typical output voltage and power vs. time in the prototype finger with  $w = 500 \mu\text{m}$ : (a)  $D = 1.0 \text{ mm}$  and (b)  $D = 1.2 \text{ mm}$ .

end of IDE structure. That the output voltage increases with velocity can be understood from the smallest time scale related to motion being on the order of 10 ms, while the electrical time constant is on the order of 0.1 ms, so the electrical subsystem is enslaved by the mechanical subsystem and  $V = RI \sim R[C_{\text{total}}(x)V_{\text{open circuit}}(x)]v$ . The output voltage depends on the diameter of the droplet. The maximum output powers for single droplets with diameters at 1.0 mm and 1.2 mm were around  $0.13 \mu\text{W}$  and  $0.18 \mu\text{W}$ , while the mean output powers for one traversal of the IDE were 5.12 nW and 7.78 nW, respectively.

If we consider a cyclic tilting of the device such that one traversal is made in half a cycle, we find that the measured result for the 1.2-mm mercury droplet corresponds to 3.0 nJ/cycle. This compares favorably to the previous work of Boland *et al.*<sup>14</sup> which demonstrated 0.17 nJ/cycle/droplet. We also note that the acceleration in our device is a modest  $0.26 \text{ g}$  as compared to  $7.2 \text{ g}$  in the previous work. In future designs, multiple droplets/marbles, each in a channel of its own, can be used in order to scale up the delivered energy.

Results from an experiment with an ionic liquid marble of diameter about  $D = 1.2 \text{ mm}$  (estimated from the volume) is shown in Fig. 5. The droplet started to slide at  $\theta \sim 12^\circ$ . Qualitatively, the output is like that for a mercury droplet, but the

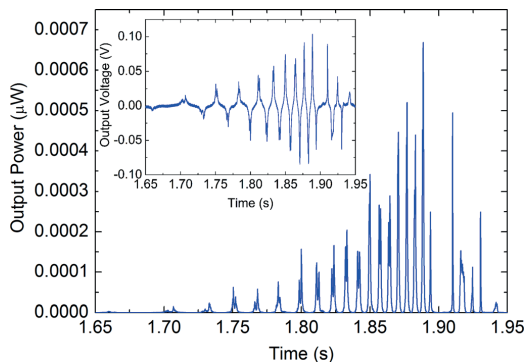


FIG. 5. Typical output voltage and power vs. time for ionic liquid marble in the prototype.

output voltage for the ionic liquid marble is smaller by about a factor ten. The difference in angle can only account for about 20% of the reduction. The conductivity of the liquid is  $\sigma = 1.4 \text{ S/m}$ ,<sup>19</sup> giving a droplet resistance  $\sim 1 \text{ k}\Omega$  which is too small to give such an effect. The shape is slightly oblate compared to the mercury droplet and could possibly be responsible for some differences; however it is difficult to reconcile with an order of magnitude negative effect. The PTFE powder on the marble have particle sizes on the order of half the film thickness and will not constitute a dense layer of material. It can, therefore, substantially increase the effective gap between the marble and the IDEs, thereby reducing the variable capacitance and the open circuit voltage, consequently causing a lower output.

Mercury has a low vapor pressure<sup>20</sup> around 0.2 Pa at room temperature, while the vapor pressure of EMIM BF4 at room temperature is practically zero ( $6.41 \times 10^{-26} \text{ Pa}$ ).<sup>21</sup> These low vapor pressures make the present device concept particularly suited for future hermetic encapsulation with vacuum in the enclosure. Vacuum enclosure is crucial in order to allow reduced cavity dimensions without excessive gas damping of droplet motion and is well established even with low temperature processes.<sup>22</sup>

In summary, an electrostatic energy harvester utilizing a conductive droplet and a thin film electret has been demonstrated in this letter. The device's improved performance was made possible by exploiting the thin films achievable with microfabrication in a process flow where all steps, except encapsulation, were planar processes on a single wafer. The electret was charged in the sputter-deposition step without need for any further charging process and proved sufficient to provide output voltages exceeding 1 V and an output energy per cycle per droplet more than a factor 17 over previous results.

Further investigations on how the operating parameters of the RF sputtering influence the charge density in the PTFE film and how performance varies with respect to electret film thickness, droplet properties, and electrode geometry are interesting topics for future work.

This work was supported by the Research Council of Norway under Contract No. 191282. Useful discussion

with Professor Atle Jensen, Professor E. M. Yeatman, and Dr. M. Löhndorf are gratefully acknowledged. We thank Mr. Yulong Zhang and the MEMS Research Center of Xiamen University, China, for PTFE sputtering of the prototype.

- <sup>1</sup>R. Bogue, *Sens. Rev.* **29**(3), 194 (2009).
- <sup>2</sup>E. Romero, R. O. Warrington, and M. R. Neuman, *Physiol. Meas.* **30**, R35 (2009).
- <sup>3</sup>G. M. Sessler, *Electrets*, 3rd ed. (Laplacian, California, 1998).
- <sup>4</sup>Y. Suzuki, *IEEE Trans. Electr. Electr.* **6**, 101 (2011).
- <sup>5</sup>S. P. Beeby, M. J. Tudor, and N. M. White, *Meas. Sci. Technol.* **17**(12), R175 (2006).
- <sup>6</sup>P. D. Mitcheson, E. M. Yeatman, G. K. Rao, A. S. Holmes, and T. C. Green, *Proc. IEEE* **96**(9), 1457 (2008).
- <sup>7</sup>L. G. W. Tvedt, D. S. Nguyen, and E. Halvorsen, *J. Microelectromech. Syst.* **19**(2), 305 (2010).
- <sup>8</sup>S. D. Nguyen and E. Halvorsen, *J. Microelectromech. Syst.* **20**(6), 1225 (2011).
- <sup>9</sup>M. E. Kiziroglou, C. He, and E. M. Yeatman, *Electron. Lett.* **46**(2), 166 (2010).
- <sup>10</sup>M. E. Kiziroglou, C. He, and E. M. Yeatman, *IEEE Trans. Ind. Electron.* **56**(4), 1101 (2009).
- <sup>11</sup>H. Lo and Y.-C. Tai, *J. Micromech. Microeng.* **18**, 104006 (2008).
- <sup>12</sup>Y. Naruse, N. Matsubara, K. Mabuchi, M. Izumi, and S. Suzuki, *J. Micromech. Microeng.* **19**, 094002 (2009).
- <sup>13</sup>R. T. Borno, J. D. Steinmeyer, and M. M. Maharbiz, *Appl. Phys. Lett.* **95**(1), 013705 (2009).
- <sup>14</sup>J. S. Boland, J. D. M. Messenger, K. W. Lo, and Y. C. Tai, in *Technical Digest: 18th IEEE International Conference on Micro Electro Mechanical Systems, MEMS 2005*, Miami, FL, 30 January-3 February, 2005 (IEEE, 2005), pp. 618-621.
- <sup>15</sup>T. Krupenkin and J. A. Taylor, *Nat. Commun.* **2**, 448 (2011).
- <sup>16</sup>M. Lohndorf, T. Kvisteroery, H. Theuss, and B. Blixhavn, US patent application 2009/0080138A1 (2009).
- <sup>17</sup>M. Armand, F. Endres, D. R. MacFarlane, H. Ohno, and B. Scrosati, *Nature Mater.* **8**, 621 (2009).
- <sup>18</sup>L. Gao, and T. J. McCarthy, *Langmuir* **23**, 10445 (2007).
- <sup>19</sup>Y.-H. Yu, A. N. Soriano, and M.-H. Li, *J. Chem. Thermodyn.* **41**(1), 103 (2009).
- <sup>20</sup>M. L. Huber, A. Laesecke, and D. G. Friend, *Ind. Eng. Chem. Res.* **45**(21), 7351 (2006).
- <sup>21</sup>M. Seiler, C. Jork, A. Kavarnou, and W. Arlt, *AIChE J.* **50**(10), 2439 (2004).
- <sup>22</sup>C. C. Lee, C. Y. Wang, and G. Matijasevic, *IEEE Trans. Compon. Packag. Technol.* **16**, 311 (1993).

## **Paper II**

**Title:** “Capacitance variation in electrostatic energy harvester with conductive droplet moving on electret film”  
**Author:** Zhaochu Yang, Einar Halvorsen, and Tao Dong  
**Journal:** PowerMEMS2013, Journal of Physics: Conference Series  
**Year:** 2013  
**Volume:** 476  
**Number:** 1





# Capacitance variation in electrostatic energy harvester with conductive droplet moving on electret film

Z Yang, E Halvorsen<sup>1</sup>, T Dong

Department of Micro and Nano Systems Technology, Vestfold University College, Norway

E-mail: Einar.Halvorsen@hive.no

**Abstract.** This work addresses numerical finite element calculations on a droplet-based electrostatic energy harvester to reveal additional characteristics that supplement previous test results. Assumptions of 2D electrode and static droplet profile have been applied to make the simulation achievable based on the real prototype. We investigate the consequences of a uniform space charge distribution in the film. Capacitance variation and open-circuit voltage of the simulation model have been determined and display respectively maximum and minimum magnitudes when the droplet is in the middle of finger gap. The sharp variation of capacitance, during which the droplet moves from the gap centre to the finger centre, can explain the narrow peaks of output voltage seen in experiments. Additionally, the influence of droplet size on the capacitance variation is also investigated.

## 1. Introduction

Harvesting energy from the environment and converting to electric energy has been a hot spot in both scientific and engineering fields since last two decades [1]. Various energy conversion principles, such as electromagnetic, thermoelectric, piezoelectric, and electrostatic, etc., have been explored [2]. Electrostatic energy harvesters, which mainly operate on the capacitance variation, and mostly employ a mass-spring configuration, have attracted considerable attention due to their compatibility with microfabrication process. Distinguished from the conventional mass-spring configuration, the electrostatic energy harvester utilizing droplet or liquid flow has advantages for low frequency non-resonant operation [3-7].

A fluidic electrostatic energy harvester utilizing interdigital electrodes (IDEs) and a thin, charged dielectric film was demonstrated in our previous work [8]. It operates on a rolling conductive droplet causing variations in the capacitance and open-circuit potential of the device's electrical port, and thereby converting mechanical energy into electrical energy when a load is connected. The detailed experimental characterization supported by a phenomenological lumped model was performed with the prototype and is presented in [9]. However, due to lack of available experimental data on the distribution of fixed charges in the film and on the possible deformation of the droplet in the inhomogeneous electric field, as well as the serious obstacles to analytical treatment of the electrostatics in the complicated structure, essential details that would be useful for further developments are not known.

<sup>1</sup> To whom any correspondence should be addressed.



To provide better understanding of this type of device, we investigate the droplet-based energy harvester concept by finite element analysis (FEA), so as to extract more features of this type of energy harvester that can't be obtained from the experimental results directly.

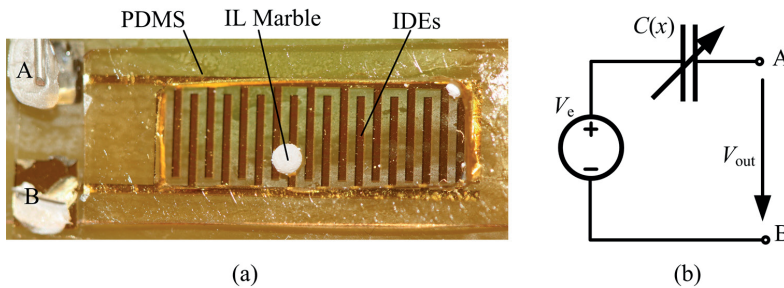
## 2. Modelling and simulation method

### 2.1. Model description

The droplet based electrostatic energy harvester (as shown in Figure 1a) can be modelled by a simple equivalent circuit (Figure 1b). The embedded charges inside the thin insulation film give rise to the voltage source  $V_e$ , while the resultant capacitance from the two terminals of the interdigital electrodes involving the conductive droplet can be simplified as a variable capacitance. Thus the relation between the embedded potential and the terminal potential can be expressed by,

$$V_{\text{out}}(x) = V_e(x) + Q(x)/C(x) \quad (1)$$

As the droplet moves across the thin film, the resultant capacitance varies in pace with the droplet displacement with respect to IDE fingers.



**Figure 1.** Droplet-based electrostatic energy harvester. (a) Optical photo of prototype; (b) Equivalent circuit characterizing the energy harvester.

### 2.2. Simplifying assumptions

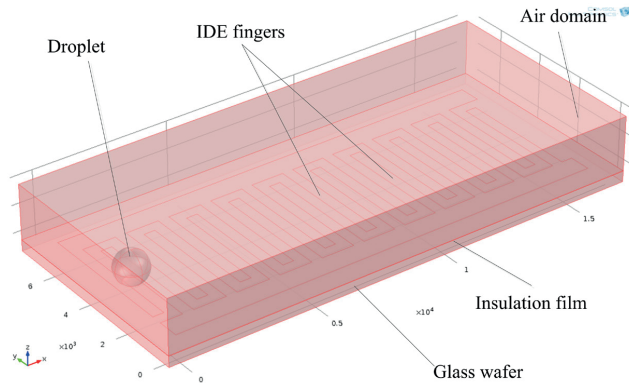
The device has greatly varying length scales within it, posing serious challenges for FEA meshing, i.e. 100nm metal film thickness, micrometre scale film thickness, millimetre scale of droplet/electrode pattern and centimetre scale device dimensions. With the technical difficulties of meshing considered, the following assumptions were applied in the model to make FEA achievable:

- the IDE finger is treated as 2D structure with zero thickness;
- the variation of droplet profile due to the droplet dynamics or electrostatic forces has been neglected;
- and the droplet is simplified as a spherical cap with a circle contact area on the dielectric film.

As the thickness of IDE finger is rather small compared with the thickness of insulation film, the 2D model can reduce the meshing difficulty but without losing the transducing feature of IDE. And the simplifications on the droplet profile actually characterize a static droplet, without addressing the dynamic behaviour. Therefore, these assumptions are reasonable. In addition, the charge distribution in the thin film is not known. As a first investigation we therefore consider a uniform space charge density and investigate its consequences.

### 2.3. Simulation domain

The simulation domain is depicted in Figure 2. The droplet was treated as a conductor and PTFE was used as the insulation film. The detailed geometrical parameters are listed in Table 1.



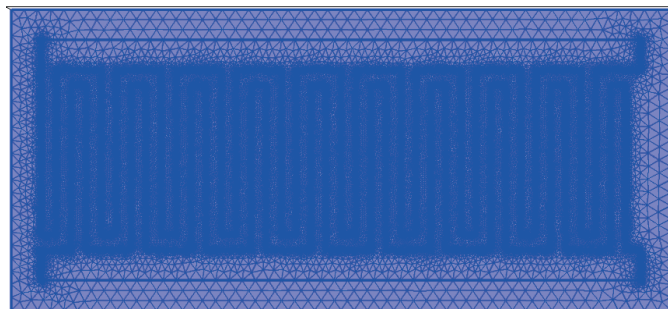
**Figure 2.** Schematic drawing of simulation domain.

**Table 1.** Parameters of the simulation domain.

Parameters	Unit	Value
Finger width of IDE	$\mu\text{m}$	400
Finger gap of IDE	$\mu\text{m}$	400
Number of finger pair	—	10
Droplet size	$\mu\text{m}$	1200
Insulation film thickness	$\mu\text{m}$	2
Glass substrate thickness	$\mu\text{m}$	400
Thickness of air domain	$\mu\text{m}$	2000

The calculation was conducted by the MEMS module of the commercial software COMSOL Ver. 4.3. Charge conservation was set for the whole simulation domain with 0-V boundary on the outer surface of the domain and also on the bottom surface of the glass substrate so as to match with practical testing where the device was placed on a conducting surface.

In order to obtain the capacitance variation with respect to the droplet displacement, a particular fine mesh was generated for IDE fingers and the thin film, as illustrated in Figure 3. As an aid in the difficult meshing of the thin film structure, virtual surfaces were used to control the mesh generation.



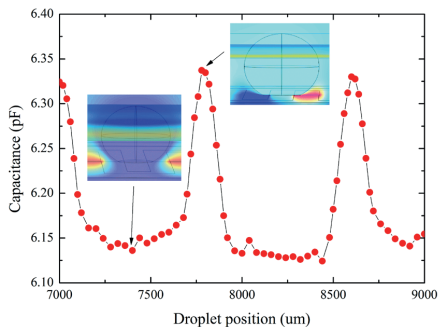
**Figure 3.** Meshing of the IDE fingers and thin insulation film (top view).

While the droplet moves along the central axis ( $x$ -direction) of the simulation domain, the capacitance was determined by applying 1.0V and 0V on the two terminals (A and B), respectively. The variation of the open-circuit potential of the prototype was checked by setting terminal A to zero charge while keeping terminal B grounded. Finally, the short-circuit charges on each electrode were checked by setting both to ground. A uniform space charge density was arbitrarily set at  $-1.0 \text{ C/m}^3$  for the insulation film. This is meaningful as the electrostatics is linear and only a scaling is necessary to correct the result to another value of embedded charge.

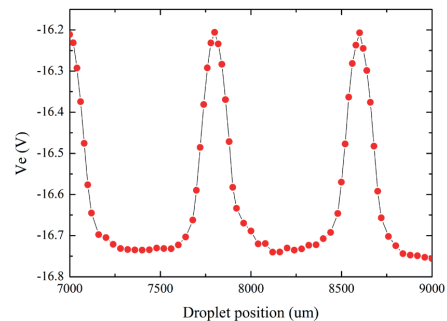
### 3. Results and discussion

#### 3.1. Capacitance variation and open-circuit voltage

Figure 4 and Figure 5 plot the variations of the capacitance and open-circuit voltage with respect to the droplet position, respectively. It is noted that the maximum values occur at the positions where the droplet is right in the middle of the two adjacent fingers (gap center) while the minimums are corresponding to the positions where the droplet are sitting right on the top of one finger (finger center). Moreover, the capacitance varies sharply as the droplet moves from the gap center towards the finger centre, which can explain why the narrowly peaked output voltage appears in the test results [9]. According to Figure 4, the range of capacitance variation in the energy harvester is not so impressive for a droplet having a diameter of 1.20 mm, less than 0.2 pF. For the real prototype, the thickness of insulation layer was smaller, down towards 1.0 micron, thus the capacitance variation is larger.



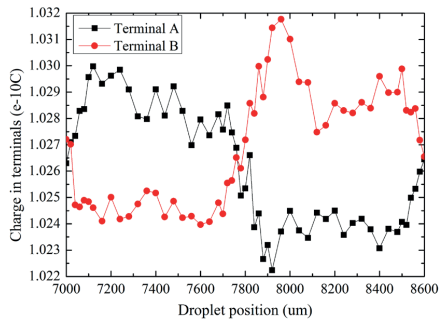
**Figure 4.** Capacitance variation with droplet position.



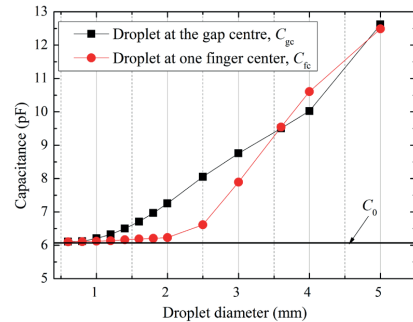
**Figure 5.** Open-circuit potential variation with droplet position

#### 3.2. Charge variation on the grounded electrodes

Figure 6 plots the charge distribution on the two terminals under grounded condition with the droplet moving within one period (four times of finger width) of IDE configuration. Due to computational errors, there are considerable fluctuations in the result. The reason for the small variations, in the third decimal, is cancellation which can be verified by calculating short-circuit charge as the product of the results in figures 4 and 5 and gives a variation that drowns in numerical error (not shown). The peak in the open circuit potential of figure 4 is a notch in its magnitude that nearly cancels the corresponding peak in the capacitance. However, figure 6 still indicates some tendency of the charge variation with respect to the droplet position: the charge variations on the two terminals alternate and reach nearly the same value at the positions when the droplet is at the gap centre. This is also where the change is largest which would give peaks in the derivative of the short-circuit charge that alternate with the period shown in the experiments. Therefore, a uniform charge distribution in the film seems to be able to qualitatively account for the observed behaviour, but numerical accuracy needs improvement to make a quantitative test.



**Figure 6.** Charges on the grounded electrodes.



**Figure 7.** Influence of droplet size on the capacitance variation.

### 3.3. Influence of droplet size on the capacitance variation

The influence of droplet size upon the capacitance is plotted in Figure 7, in which the droplets hold a constant contact angle of  $60^\circ$  with both positions at gap centre (gc) and finger centre (fc). It is clear that for the IDE with finger/gap width of  $400\mu\text{m}$  ( $C_0=6.09\text{pF}$ ), the total capacitance variation ( $\Delta C=C_{gc}-C_{fc}$ ) increases rapidly with the droplet size, and has a maximum of  $1.4\text{pF}$  for a droplet size of  $2.5\text{mm}$ . The variation drops as the droplet size keep increasing, even turns to negative when the droplet covers more than one pair of fingers. This indicates that the droplet size should be matched well to the IDE pitch and could favourably have been considerable larger than what was used in the previous experiments. The finding explains why a bigger droplet gave larger output in test [9].

## 4. Conclusions

Based on a previous prototype of a droplet-based energy harvester, a FEA model was built by adopting several simplifying assumptions. Numerical calculations were used to obtain variations of capacitance, open-circuit voltage and short-circuit charge by setting different boundary conditions. The findings are qualitatively consistent with the voltage peaks related to the short-circuit charge in previous tests. The numerical accuracy of the short-circuit charge needs improvement for performance estimates. It is of interest to further study the effect of charge variations in the film. It is also found that droplet size should match with IDE pitch to have a larger capacitance variation.

## Acknowledgement

This work was supported by Research Council of Norway under Contract No.191282.

## References

- [1] Bogue R 2009 *Sensor Rev.* **29** 194
- [2] Mitcheson P D, Yeatman E M, Rao G K, Holmes A S and Green T C 2008 *Proc. IEEE* **96** 1457
- [3] Boland J S, Messenger J D M, Lo K W, and Tai Y C 2005 *Technical Digest: 18th IEEE International Conference on Micro Electro Mechanical Systems* 618
- [4] Krupenkin T and Taylor J A 2011 *Nat. Commun.* **2** 448
- [5] Löhndorf M, Kvisteroery T, Theuss H, and Blixhavn B 2009 *US patent application* US 2009/0080138A1
- [6] Choi D-H, Han C-H, Kim H-D and Yoon J-B 2011 *Smart Mater. Struct.* **20** 125012
- [7] Bu L, Wu X, Wang X and Liu L 2013 *J. Intel. Mat. Sys. Str.* **24** 61
- [8] Yang Z, Halvorsen E and Dong T 2012 *Appl. Phys. Lett.* **100** 213905
- [9] Yang Z, Halvorsen E and Dong T 2013 *J. Microelectromech. S.* DOI: 10.1109/JMEMS.2013.2273933



## **Paper III**

**Title:** “Electrostatic energy harvester employing conductive droplet and thin-film electret”  
**Author:** Zhaochu Yang, Einar Halvorsen, and Tao Dong  
**Journal:** Journal of Microelectromechanical Systems  
**Year:** 2014  
**Volume:** 23  
**Number:** 2  
**Pages:** 315-323





## **Paper IV**

**Title:** "Identification of microfluidic two-phase flow patterns in lab-on-chip devices"  
**Author:** Zhaochu Yang, Tao Dong, and Einar Halvorsen.  
**Journal:** Bio-medical Materials and Engineering  
**Year:** 2014  
**Volume:** 24  
**Number:** 1  
**Pages:** 77-83



## Paper V

**Title:** “Integratable Capacitive Sensor for Identification of Microfluidic Two-phase Flow Pattern in Lab-on-chip”

**Author:** Zhaochu Yang, Tao Dong, Atle Jensen, and Einar Halvorsen.

**Journal:** *Submitted to Journal of Microelectromechanical Systems*

**Year:** 2014

**Number:** 2014-0360

